USE OF HYBRID AIRFOIL DESIGN IN ICING WIND TUNNEL TESTS OF LARGE SCALE SWEPT WINGS

BY

ANDREW J. MORTONSON

THESIS

Submitted in partial fulfillment of the requirements
for the degree of Master of Science in Aerospace Engineering
in the Graduate College of the
University of Illinois at Urbana-Champaign, 2012

Urbana, Illinois

Adviser:

Professor Michael B. Bragg

Abstract

In-flight ice accretion is an important safety consideration for modern aircraft. The certification of commercial airliners for flight into known icing is difficult due to the expense and challenge in finding the desired icing conditions in flight. The large size of commercial aircraft relative to existing icing wind tunnels and lack of robust scaling methods also makes ice accretion wind tunnel testing difficult. Hybrid or truncated airfoil models use full-scale leading edges with redesigned aft sections to provide test articles with much reduced model chord and therefore tunnel blockage allowing effectively full-scale icing testing on very large wings. This thesis presents research focused on understanding the accuracy of hybrid designed models applied to the design of models for swept wing commercial airliners. Research was performed examining the effect of the hybrid scale factor, extent of the full-scale leading edge, application of a flap, wind tunnel walls, and variation of icing conditions. Hybrid designs were found to be dependent on the design angle of attack and ice accretion parameter, but they did provide an accurate ice shape. While limits to the flap effectiveness exist, flaps can be used to match ice shapes for off-design cases at low and moderate angles of attack. The tunnel wall analysis shows that there are some aerodynamic effects due to the wind tunnel walls, but the droplet impingement remained similar, implying that the hybrid design is not highly dependent on tunnel walls for wind tunnel height to airfoil chord (h/c) ratios greater than two.

Acknowledgments

I would like to thank Prof. Michael Bragg for giving me the opportunity to participate in this research and guidance and support throughout the process. I would also like to thank Prof. Eric Loth and Chris Triphahn who worked assisted in investigations of hybrid designs through CFD methods. I would also like to thank NASA for funding this research and Andy Broeren, Mark Potapczuk and the rest of the icing research branch for their advice on this process. I would also like to thank Jeff Diebold and Phil Ansell, who did preliminary research in these areas and taught me how to use some of the codes and processes, as well as Paul Schlais and Brian Woodard for their help in running some of the cases in LEWICE 2D. Finally I would like to thank my parents John and Connie Mortonson and my fiancée Hannah Nelson, who have supported me through the entire process.

Table of Contents

Table of Symbols and Abbreviations vi

Table of Figures vii

I. Introduction 1

- A. Hybrid Airfoil Design 1
- B. Ice shape classification and aerodynamic research 3
- C. Research Objectives 5

II. Research Methods 7

- A. Selection of 2D Airfoils for Hybrid Design 7
- B. Airfoil Analysis 9
  - 1. XFLR5/XFOIL 9
  - 2. LEWICE 2D 10
- C. Hybrid Airfoil Design 11
  - 1. PROFOIL Airfoil Design 11
  - 2. Alternative Hybrid Designs 12
  - 3. Hybrid Airfoil Analysis 13

III. Results and Discussion 16

- A. Initial Baseline Hybrid Design 16
- B. Studies of Hybrid Design Parameters 17
  - 1. Sensitivity study of Hybrid Design Parameters 17
  - 2. Leading-Edge Chordwise Extent 22
  - 3. Hybrid Scale Factor (SF) 26
- C. Hybrid Design for Varied Conditions 29

1. Variation in Full-Scale Chord 29

2. Variation in Angle of Attack 34

3. Circulation and Stagnation Point Matching 35

4. Variation in Icing Conditions 39

D. Use of Flap in the Hybrid Design Method 40

1. Comparison of symmetric flapped and cambered hybrid design 41

2. Use of flap for off-design conditions 44

E. Effects of Tunnel Walls on Airfoil Ice Accretion 47

1. Aerodynamic corrections and wind tunnel blockage 47

2. Tunnel Effects on C_P 49

3. Tunnel Effects on Droplet Impingement 53

4. Design in the Presence of Walls 56

IV. Summary, Conclusions, and Recommendations 58

A. Summary 58

B. Conclusions 58

C. Recommendations 59

Appendix A List of Airfoil Coordinates for CRM Sections 61

Appendix B List of test cases and design variables 64

References 65

Table of Symbols and Abbreviations

A	Wind Tunnel Area
α	Airfoil Angle of Attack
α_D	Hybrid Design Angle of Attack
α_{nose}	Hybrid Nose Angle of Attack
β	Collection Efficiency
β_{max}	Maximum Collection Efficiency
c_0	Reference Chord (Full Scale)
c_{fs}	Full Scale Chord
c_{hyb}	Hybrid Airfoil Chord
C_P	Pressure Coefficient
C_d	Drag Coefficient
C_l	Lift Coefficient
C_{m0}	Zero lift Moment Coefficient
CFD	Computational Fluid Dynamics
CRM	Common Research Model
CRM65	65% Scaled Common Research Model
D	Drag on Body
ε^{total}	Total Blockage Estimate
ε^{sb}	Solid Blockage Estimate
ε^{wb}	Wake Blockage Estimate
FAA	Federal Aviation Administration
F_r -	Froude Number
Δf -	Change in Flap Deflection, Positive Down
γ	Vorticity Distribution
Γ	Airfoil Circulation
$\bar{\Gamma}$	Non-Dimensional Airfoil Circulation
K	Droplet Inertia Parameter
L	Lift on Body
m	Mass of Body
MVD	Median Volume Droplet Diameter
ONERA	Office National d'Etudes et de Recherches Aerospatiales
Ψ	Two-Dimensional Stream Function
R_u	Droplet Reynolds Number
SF	Hybrid Scale Factor
σ	Source Distribution
s/c_0	Normalized Surface Length Coordinate
T	Free-Stream Temperature
U_∞	Free-Stream Velocity
u_∞	Horizontal Free-Stream Velocity
V	Model Volume
v_∞	Vertical Free-Stream Velocity
x	Horizontal Coordinate
x/c_0	Normalized Horizontal Coordinate
y	Vertical Coordinate
y/c_0	Normalized Vertical Coordinate

Table of Figures

Fig. 1.1 Geometric input variables for the hybrid airfoil design... 2

Fig. 1.2 Hybrid design parameters on a α_D = 2° hybrid design.. 2

Fig. 1.3 CRM65 semi-span wind tunnel model tested at the University of Illinois..................................... 5

Fig. 2.1 CRM wing sections superimposed on Illinois CRM model... 7

Fig. 2.2 Perpendicular airfoil cuts and stream-wise locations.. 8

Fig. 2.3 22%, 60%, and 90% perpendicular airfoil section cut... 9

Fig. 2.4 90% span symmetric flapped hybrid (Δf=12°) and cambered hybrid (α_D=4°) designs................... 13

Fig. 2.5 Example Cp plot for a hybrid airfoil (60%, α_D=2°)... 14

Fig. 2.6 Example β distribution (60% span, α_D=2°). 15

Fig. 2.7 Example ice shape with labeled characterization parameters (60% span, α_D=2°)....................... 15

Fig. 3.1 Initial baseline hybrid design compared to the full-scale airfoil. 17

Fig. 3.2 Sensitivity analysis for changing nose droop on the (a) hybrid airfoil design and (b) LEWICE predicted ice shape.. 18

Fig. 3.3 Effect of change in C_{m0} on (a) hybrid airfoil shape and (b) LEWICE predicted ice shapes..... 20

Fig. 3.4 C_P plots for variation in (a) nose droop and (b) C_{m0}... . 21

Fig. 3.5 Adjustments to nose droop and zero lift moment coefficient on airfoils with equal x/c and y/c scales 22

Fig. 3.6 Hybrid airfoils with varied lower-surface leading-edge extents... .. 23

Fig. 3.7 Ice shapes for lower surface leading-edge extents varied from 3% to 15% full-scale chord............. 24

Fig. 3.8 Droplet impingement curves for variation in lower surface leading-edge extent......................... .. 24

Fig. 3.9 C_P distributions for 60% span CRM 65 airfoil with varying lower-surface leading-edge extents...... 25

Fig. 3.10 Hybrid airfoils with varied hybrid scaling factors.. 26

Fig. 3.11 Ice shapes for hybrid designs with varied scaling parameters... .. 27

Fig. 3.12 Collection efficiency (β) for varied hybrid scaling parameters... .. 27

Fig. 3.13 Inviscid and viscous C_p plots for full scale airfoil and SF = 3 and SF = 5 hybrid airfoils at α_D=2°... .. 28

Fig. 3.14 60% span CRM airfoil and hybrid design... 30

Fig. 3.15 22% Span CRM and hybrid airfoils.. 30

Fig. 3.16 (a) ice shape and (b) collection efficiency for the 22% span CRM full scale and hybrid.......... 31

Fig. 3.17 90% span CRM airfoil and hybrid designs.. 32

Fig. 3.18 Comparison of the 90% span full-scale and hybrid airfoils of (a) ice shape and (b) β distributions ... 33

Fig. 3.19 Full-scale mid-span CRM airfoil and four hybrid designs for varied angles of attack............ 34

Fig. 3.20 Hybrid designs for (a) α_D=0°, (b) α_D=2°, (c) α_D=4°, and (d) α_D=6°... ... 35

Fig. 3.21 Designs for α_D = 2°, varied to match leading edge droplet impingement........................... 37

Fig. 3.22 C_P plots for the three designs at α = 2°.. 37

Fig. 3.23 Ice shape comparison between the standard hybrid and stagnation point matched designs........... ... 38

Fig. 3.24 Droplet impingement distributions for matched stagnation point and matched ice hybrid designs ... 38

Fig. 3.25 Ice shape generated at -13° F for the 60% CRM airfoil full scale and hybrid................................ ... 39

Fig. 3.26 Ice accretion for 20μm droplets on the full scale and hybrid 60% span CRM airfoil.................... ... 40

Fig. 3.27 Hybrid cambered and symmetric flapped designs for the CRM 60% span airfoil.............................. 42

Fig. 3.28 Ice shapes comparing cambered and symmetric flapped hybrid designs at α_D=2°....................... ... 43

Fig. 3.29 Comparisons of ice shapes for hybrid designs at α_D = 6°... 44

Fig. 3.30 α = 0° ice shapes for full scale, α_D=0° cambered design, and α_D=2° cambered and flapped designs. 45

Fig. 3.31 α = 6° ice shapes for full scale, α_D=6° cambered design, and α_D=2° cambered and flapped designs. 46

Fig. 3.32 Full scale and hybrid ice accretions for α = 4°, with off design hybrid corrected with angle of attack adjustment... 47

Fig. 3.33 C_P plots for the CRM 60% span hybrid with tunnel wall effects... 50

Fig. 3.34 Changes in C_P distribution for increasing wall effects...... 51

Fig. 3.35 Tunnel wall effects on the C_P for the (a) full scale 60% span and (b) hybrid airfoils.................. .. 52

Fig. 3.36 Tunnel wall effects for CRM hybrid airfoils at angles of attack from 0° to 6°............................ .. 53

Fig. 3.37 Collection efficiency for CRM 60% span airfoil and scale factor 3 hybrid................................ ... 54

Fig. 3.38 Collection efficiency for the CRM hybrid airfoil at (a) low and (b) high tunnel blockage.......... ... 55

Fig. 3.39 Tunnel effects on hybrid C_P distribution with corrected flapped hybrid design.......................... ... 56

Fig. 3.40 β distribution for the hybrid design in tunnel and flapped ‘corrected’ design.................... 57

I. Introduction

Airframe icing has been a topic for aircraft safety research since at least the 1930s, but detailed analysis of the flowfield created by ice accretions began when computational fluid dynamic codes were applied to the problem in the late 1970s.[1] Much of the research in support of in-flight icing has been applied to characterizing two-dimensional airfoil ice shapes. Research toward the understanding of ice shapes and aerodynamic effects for three-dimensional wings is still developing, especially for wings with significant sweep or taper. Modern wings are far too large to test at full scale in existing icing tunnels, but the icing problem is too complex to rely on computational models alone for certification. Ice accretion scaling methods exist and are well-documented for models that are too large, or are limited by the available tunnel speed or droplet size.[2] Ice accretion scaling methods cannot be extended well to high scale factor designs. Thus full-scale icing conditions are preferred for testing, especially when full-scale hardware, like icing protection systems, need to be tested. In order to produce accurate ice shape results for large swept wings in icing tunnels, hybrid scaling techniques are an attractive option to reduce chord length and tunnel blockage to improve the accuracy of the simulation.

A. Hybrid Airfoil Design

Research in truncated airfoils for icing research began in the 1950's. The truncated design started from a full-scale airfoil, maintained a portion of the full-scale leading edge geometry, and added a simple fairing or flap on to the back. These flapped airfoil designs showed that a truncated airfoil can match ice shapes generated on full-scale airfoils.[3] As airfoil technology advanced and the requirements for icing testing became more extensive, advanced design methods for aft sections and flaps was required. A systematic method was needed to consistently generate truncated airfoils.

The hybrid design method was developed in 1997 by Saeed, Selig, and Bragg[4] with the help of Selig's PROFOIL, a multipoint inverse airfoil design code.[5] This method provides a simple program to design truncated airfoils that match the leading-edge flowfield and droplet impingement through the adjustment of specific input variables. Three geometric input variables control the main design of the hybrid airfoil: the hybrid scale factor and the upper and lower leading edge extents as seen in Fig. 1.1. These geometric input variables are set for all hybrid airfoil designs, but the method is only well-documented for hybrid scale factors up to two.[4] Advanced cambered hybrid designs have additional design variables that determine the aft section coordinates. The nose droop is the angle between the full-scale leading-edge chord line and the trailing edge chord line; it is generally negative, between 0 and -5 degrees, and decreases as the design angle of attack increases and shown in Fig. 1.2. The aft camber is controlled by setting the moment coefficient at alpha = 0, C_{m0}, which is generally between 0 and -0.5, and also decreases with increasing angle of attack. Generally both nose droop and C_{m0} are increased simultaneously to prevent either design parameter to increase to a level which would cause increased risk of separation. The effects of the two parameters on airfoil shape are shown in Fig. 1.2.

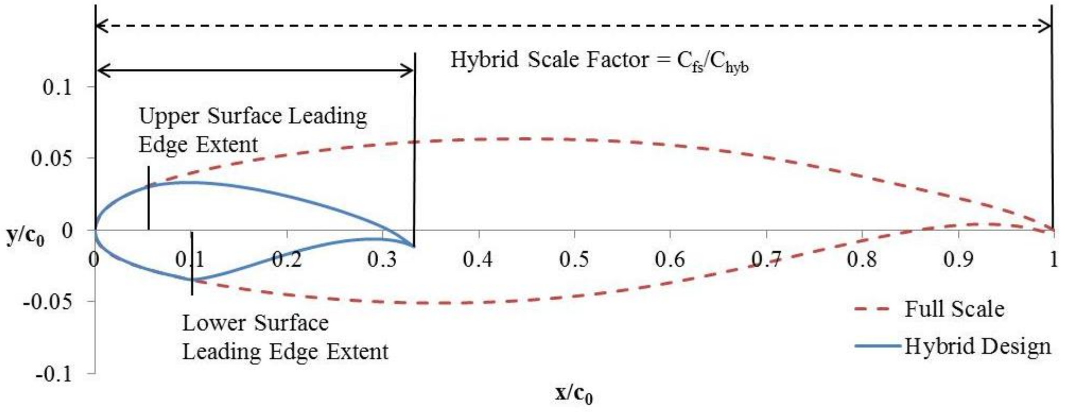

Fig. 1.1 Geometric input variables for the hybrid airfoil design.

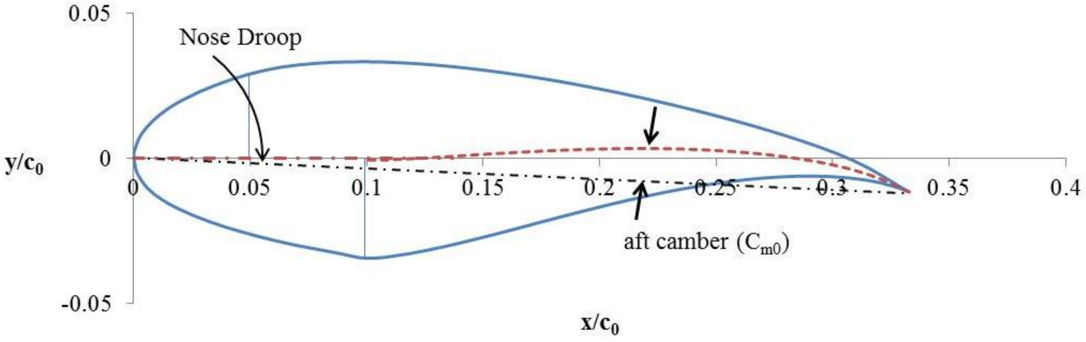

Fig. 1.2 Hybrid design parameters on a α_D = 2° hybrid design.

A hybrid airfoil is designed to reproduce full scale leading-edge flowfield and droplet impingement at a specific angle of attack. The method uses a newton iteration method to adjust a subscale design to match the given C_{m0} value and nose droop for the hybrid design. The leading-edge local velocity distribution and stagnation point of the hybrid design is compared to the full-scale to evaluate the hybrid design.[4] The AIRDROP[6] generated collection efficiency is also used for a given set of icing conditions. The icing conditions are given to AIRDROP, a code that generates the droplet trajectories and impingement on an airfoil, as the droplet Reynolds number, R_u, the Froude number, F_r, and the droplet inertia parameter, K.[4] These parameters determine the effects of droplet size, freestream velocity, airfoil chord, and gravity on the droplet trajectories. Hybrid designs were generated and tested by Saeed for a scale factor between 1.1 and 2. At these low scale factors, the circulation was reduced by 2-5% from the full-scale for designs with zero nose droop. These observations lead to the conclusion that the full scale circulation was nearly matched by the hybrid design. Designs which included nose droop saw a reduction in circulation of up to 11%.[4]

Generally it is not practical for models to be built at each angle of attack for the single point design. A design method was proposed to add a simple 20% chord flap to the scale factor 2 hybrid design.[7] The addition of a flap allowed the hybrid airfoil to predict ice shapes over a range of angles of attack. Flapped designs were shown to be limited for high angles of attack as the flap deflection increased. The flap design also showed a nearly constant percentage reduction in circulation from the full scale over a range of angles of attack.[7] Advanced slotted flaps can further increase the effective range of angles of attack. A model was built based on these early airfoils and tested in the Icing Research Tunnel at NASA Glenn.[8] The hybrid model and its full scale counterpart were tested at angles of attack from 0° to 8°. The results of this experimental validation showed that the ice shapes on the hybrid design were qualitatively similar to ice shapes on full-scale airfoils.[8]

B. Ice shape classification and aerodynamic research

Design and certification of aircraft to protect against icing related accidents requires the geometry of accreted ice for aerodynamic testing. Facing limited aircraft performance data in icing conditions, NASA partnered with the University of Illinois and ONERA to generate ice shapes and test aerodynamic performance. The Airfoil Ice Accretion Aerodynamics Simulation project, referred to as the Sunset project, tested the NACA 23012 airfoil with a range of ice accretions.[9] The six phase project began by defining four classifications of ice shapes, ice roughness, horn ice, streamwise ice, and spanwise ridge ice. These four types of ice, generated in differing conditions, were tested on an 18 in. chord model in the Illinois 3 ft. by 4 ft. tunnel and then on a 72 in. model in the ONERA F1 tunnel.[10] These tests provided valuable data for ice accretion testing and certification.

To continue this research, a new project was initiated to develop and test ice accretions on a three-dimensional wing model as was done for the NACA 23012. The project will develop ice shapes on a modern transonic swept wing representative of a wing on a commercial transport aircraft. The wing selected for this project was the Common Research Model (CRM) wing, designed by individuals at Boeing and NASA for the NASA subsonic fixed wing technical working group.[11] The wing design was selected for the FAA project because it was typical of most modern wide-body commercial transport designs and had significant three-dimensional flow features. The model geometry is also fully available to the public and has both computational and experimental data published. The CRM has been tested in the NASA Ames 11-ft wind tunnel as well as the National Transonic Facility,[12] and future tests are planned for other international facilities. Recently, the fourth and fifth Drag Prediction Workshops used the geometry to validate computational results. While most of these results are transonic, and ice accretion is generally a subsonic phenomenon, the CRM is becoming widely used in the aerodynamic research community. The Common Research Model was designed for a cruise Mach number of 0.85 at a Reynolds number of 40 million, with an aspect ratio of 9.0 and taper ratio of 0.275.[11] The CRM wing had a span of 192.8 ft, and a chord of 39 ft at the side of body.

To generate full-scale ice accretions for testing in the F1 tunnel, the 192 ft span CRM wing needed to be tested in the 6 ft by 9 ft Icing Research Tunnel. To accomplish this, a number of techniques have been investigated. First, the full-scale was reduced to a CRM65 wing, which is 65% of the original size. The CRM65 has a span of 125.3 ft and a chord of 25.4 ft at the side of body and 5.82 ft at the tip. The mean aerodynamic chord is 14.94 ft, and the wing area is 1745 ft^2. The wing is swept 35° at the quarter chord and is tapered with a Yehudi break from the root to 37% span. Figure 1.3 shows a model of the CRM65 wing used in a wind tunnel test at the University of Illinois. The CRM wing is also designed with a significant level of wash-out, and twist of 8.2 degrees from the side of body to wing tip. Spanwise sections will be modeled in the tunnel with segmented flaps to approximate the lift distribution of the full three-dimensional wing. To reduce the large model blockage and fit the CRM airfoils in the tunnel, a high scale factor truncated airfoil method was needed.

Fig. 1.3 CRM65 semi-span wind tunnel model tested at the University of Illinois.

The hybrid scaling methods for large, transport scale swept wings are not well-documented. To ensure accurate ice shape results from the Icing Research Tunnel, a complete study of hybrid methods applied to large wings was required. The hybrid scaling method reduces the chord of the airfoil, while maintaining the leading-edge pressure distribution and droplet impingement. This allows testing at full-scale icing conditions while maintaining an acceptable level of tunnel blockage. Droplet scaling methods, which reduce the model size by adjusting flowfield conditions such as airspeed, droplet size, and liquid water content to match the ice accretion, were also considered, but are only necessary for very large full scale geometry.[2]

C. Research Objectives

This investigation into hybrid scaling methods focused on modeling large-scale swept wings with full-scale chord on the order of the wind tunnel height. Testing at full-scale conditions is preferred for this kind of testing, because tests often need to be run with full-scale icing protection systems, and the accreted roughness does not scale with ice accretion scaling. In developing hybrid airfoil design methods for large swept-wing aircraft, this study had three major objectives.

- Evaluate the quality of a variety of hybrid designs and determine the accuracy of ice shapes created using hybrid designs.

- Understand the effect of flap deflection on hybrid design and determine advantages of advanced model design.
- Determine effect of tunnel walls on droplet trajectories, especially for models with high blockage.

A baseline design was created and modified to determine the effect of design parameters. These designs were all evaluated for accuracy using XFOIL, to determine the C_P distribution, AIRDROP, to determine the collection efficiency, and LEWICE, to determine the two-dimensional ice shape. Hybrid airfoils were also designed with differing scale factors, leading-edge extents, and design angle of attack. Flap designs were created from a symmetric truncated airfoil and existing designs to match ice shapes over a range of angles of attack. Finally the TUNDROP code was used to evaluate the tunnel wall effects. The C_P and calculated β distributions were compared between designs with and without tunnel wall effects.

II. Research Methods

A. Selection of 2D Airfoils for Hybrid Design

Span-wise sections for the hybrid design method were determined based on the design of the wing and the objectives of this study. The common research model had four characteristic regions of the wing, shown in Fig. 2.1. For the CRM, the inboard wing, 0% to 30% wing span, was characterized by a large chord and low camber. The ice shapes were smaller as normalized by the chord. The inboard section also generated the largest lift due to its large area and the flow having low spanwise variation. The Yehudi break region, 30% to 45% span, where the wing's taper ratio changes, was also near the strut and nacelle in configurations which included them.[11] Areas near discontinuities or wing protrusions likely see a level of three-dimensionality and cannot be well characterized by a two-dimensional analysis. Inboard sections pose a challenge for ice accretion models on tapered wings because of their significant size, which can lead to higher blockage in wind tunnel tests on the two-dimensional sections.

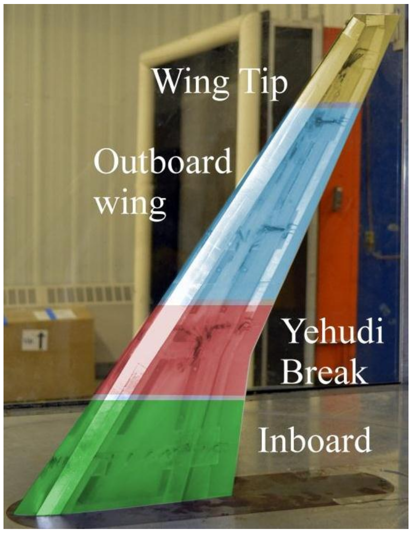

Fig. 2.1 CRM wing sections superimposed on Illinois CRM model.

Outboard wing sections often allow more freedom in the hybrid design because of their shorter chord. The outboard wing of the CRM, which extended from about 45% to 80%, had shorter chord lengths leading to more substantial ice shapes when viewed as a percent of chord. The wing tip, which consisted of the last 20% of the wing, had much shorter chords, which produced the largest ice shapes when normalized by chord. Wing tips experience highly three-dimensional flow due to wing tip vortex effects and spanwise flow.

Icing protection systems can influence the selection of wing sections as well. On some wings similar to the CRM, the system runs from the Yehudi break through the outboard region. Thus certain spanwise sections of the wing might be preferred based on characteristics of these leading-edge systems. However, Icing protection is outside of the scope of this study, so wing sections were selected here on the basis of the aerodynamic characteristics of the wing. Three airfoils were taken from the CRM that were used as examples for the hybrid design. The midchord point of these airfoils was located for the inboard airfoil at 22% span, the outboard airfoil at 60% span, and 90% span near the wing tip.

In order to provide a representative two-dimensional airfoil from a three-dimensional wing, airfoil cuts should be made normal to the leading edge of the wing, which are shown crossing the streamwise stations in Fig. 2.2. Selecting airfoils normal to the leading edge isolates the two dimensional airfoil flow from the three dimensional spanwise flow. The CRM geometry used is publicly available in a number of forms online through the 4th and 5th drag prediction workshops.[11] Extracting two-dimensional airfoils can be performed a number of ways. Using the Pro/Engineer CAD software[13], airfoil cuts for these tests were made by inserting a plane perpendicular to the leading edge of the wing, and then extracting coordinates from the intersection of the plane and wing. The airfoils that will be used in these tests are shown in Fig. 2.3 and coordinates are given in Appendix A.

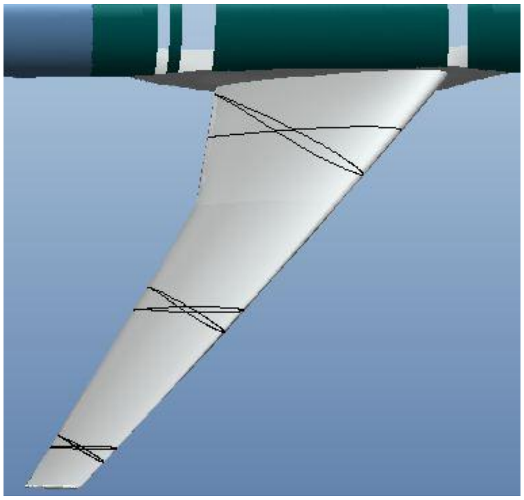

Fig. 2.2 Perpendicular airfoil cuts and stream-wise locations.

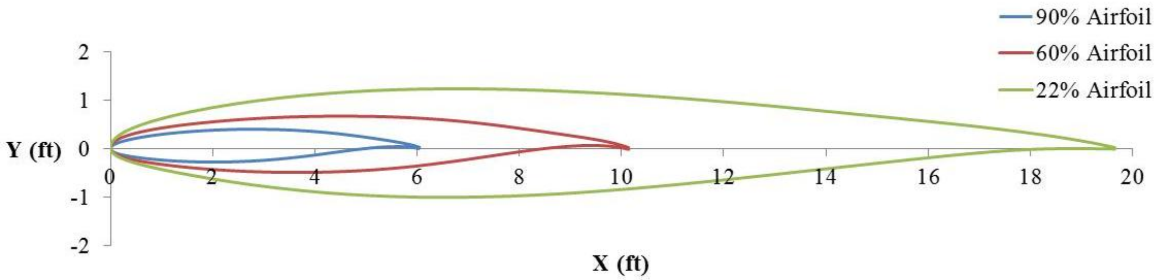

Fig. 2.3 22%, 60%, and 90% perpendicular airfoil section cuts.

B. **Airfoil Analysis**

Two tools were used to analyze airfoil aerodynamic performance and ice accretion characteristics. The XFOIL airfoil analysis code[14] was used to generate inviscid and viscous C_P curves to determine the location of the stagnation point and C_P distribution over the leading edge. The XFOIL code is run within the framework of the XFLR5 wing analysis code.[15] This code provides a user interface to run the XFOIL code and provides a simple airfoil manipulation tool. Ice accretion analysis was performed using the two-dimensional version of the LEWICE code version 2.2.[16] This code predicts droplet impingement and generates ice shapes for a given airfoil, angle of attack, and flight and icing conditions, over a given icing time.

1. *XFLR5/XFOIL*

XFOIL was developed by Mark Drela at MIT in 1986, as an airfoil analysis and design code. The code has undergone a number of improvements but has remained largely unchanged since 2001.[14] The program solves for the inviscid and viscous flowfields around the airfoil to provide C_P and integrated lift, pitching moment, and drag values. Due to the aggressive thickness and camber distribution of the hybrid airfoils, an estimate of viscous effects is useful in understanding the limitations of the design.

XFOIL's inviscid formulation generates a potential flow solution for the airfoil. Using potential flow theory, the code superimposes the free stream flow, a source distribution over the airfoil surface and wake, and a vortex distribution over the airfoil surface.[17] The airfoil is modeled with discrete flat panels with uniform source strength σ, and vortex strength γ. From these panels, the value of the stream-function, Ψ, can be calculated at any point in the flow from the following equation:

$$\Psi(x,y) = u_\infty y - v_\infty x + \frac{1}{2\pi}\int \gamma(s)\ln[dist(s:(x,y))]ds + \int \sigma(s)angle(s:(x,y))\,ds \qquad (1)^{17}$$

A system of equations is formed by setting the stream-function constant on the airfoil surface, ensuring no flow through the body. The system is solved by satisfying the Kutta condition, matching γ on the trailing edge of the upper and lower surface. Since the geometry is fully defined, and the stream function must be constant on the surface, the system of equations can be solved for the vortex distribution on the airfoil surface. The internal velocity of the airfoil is defined to be zero, so the vortex distribution can be used to calculate the surface velocity and C_P.

The viscous formulation estimates the viscous effects through the use of the integral boundary-layer method. The code provides the option of a forced transition point or transition at a critical value of n, the amplitude of the largest T-S wave.[17] The wake is treated as a single viscous boundary layer, which is part of the calculation of the viscous base drag. The boundary-layer equations are integrated and discretized at each panel and can be solved with the inviscid equations using methods described in reference 3. The predicted pressure coefficients are integrated to determine lift and moment coefficients, and drag is calculated from the integrated boundary-layer effect.

The XFLR5 program was created by André Depperois for model plane builders, as a more user friendly way to access the XFOIL code.[18] The code also incorporates a three-dimensional vortex lattice and panel method to analyze simple wings. XFLR5 has a number of tools to refine, scale, and add simple flap deflections to airfoil sections. The hybrid airfoils were each refined to 101 points through the global refinement routine. Each airfoil was analyzed using the XFOIL direct analysis portion of the program.[15] Once a flow condition is defined with a Reynolds number and Mach number, a full analysis can be performed over a range of angles of attack.

2. *LEWICE 2D*

LEWICE, the Lewis ice accretion program, is a tool developed by NASA's icing branch to predict ice shapes and collection efficiencies.[16] LEWICE performs a potential flow solution utilizing a panel method, similar to the inviscid XFOIL formulation. The code calculates droplet trajectories and collection efficiency over the airfoil surface. The droplet trajectories are calculated by numerically integrating the following equations, where γ is the angle between the particle velocity and the free stream and α is the angle of attack:

$$m\ddot{x}_P = -D\cos\gamma - L\cos\gamma + mg\sin\alpha \tag{2}$$

$$m\ddot{y}_P = -D\sin\gamma + L\cos\gamma - mg\cos\alpha \tag{3}$$

Particle lift and drag are calculated using the average droplet diameter and flow-field conditions. Then thermodynamic relations are used to determine ice shape growth, and the process is iterated with the new airfoil with ice shape geometry.[16] LEWICE requires atmospheric temperature, pressure, and velocity as well as the relative humidity, liquid water content (LWC), and droplet diameter in addition to airfoil geometry and flowfield information.

C. **Hybrid Airfoil Design**

The goal of the hybrid design process is to generate an airfoil with a much shorter chord and wind tunnel blockage that matches the ice accretion characteristics of a full-scale airfoil. The design includes a full-scale airfoil leading-edge geometry with a specially designed aft airfoil. The process uses three codes to generate a candidate airfoil that is then analyzed to determine the degree of the ice shape match, and the process can be iterated if a better match is required.

1. *PROFOIL Airfoil Design*

The first step in the process was analyzing the full-scale airfoil with XFOIL and AIRDROP. AIRDROP[6] generates an inviscid flowfield and calculates droplet trajectories and collection efficiencies. The full-scale analysis provides C_P measurements and the collection efficiency distribution (β). Using the droplet impingement limits calculated in AIRDROP and knowledge of the airfoil geometry, the user selects the upper and lower full-scale airfoil leading-edge extents to be used in the hybrid airfoil design.

The PROFOIL code was then used to design the aft section of the hybrid airfoil. PROFOIL is an airfoil design code developed by Michael Selig and modified by Farooq Saeed to generate hybrid airfoils.[19] PROFOIL starts the airfoil design with a segmented circle and modifies the geometry to conform to a prescribed velocity distribution. Additional tools allow the user to set other airfoil values, such as the pitching moment or zero-lift angle of attack, and limit the maximum camber and thickness. The two most important design variables set by the user for the PROFOIL code are the zero-lift pitching moment coefficient (C_{m0}) and the nose droop (in degrees). These two variables determine the camber of the hybrid airfoil, as well as the angle of intersection between the hybrid airfoil and the leading edge. The aft section of the hybrid airfoil is merged with the leading edge of the full-scale airfoil at the user-prescribed leading-edge extents. Once the airfoil is designed in PROFOIL, the new hybrid airfoil is analyzed with XFOIL and AIRDROP, and the resulting C_P and β distributions are presented to the user for comparison. Adjustments to C_{m0} and nose droop often need to be made to perfect the hybrid design.

Flaps are also a common tool used in designing hybrid airfoils. PROFOIL has the ability to add a simple flap to the hybrid design.[7] This allows the hybrid design to be analyzed in XFOIL and AIRDROP, but it does not factor in to the airfoil design created by the PROFOIL code. For consistency, all flaps used in this study were created using the XFLR5 program and not created in the hybrid design process. In XFLR5, flaps were added by defining the flap angle in degrees, with positive as a trailing-edge down deflection, as well as defining the hinge location as a percentage of C_0, the full scale chord, from the leading edge. The hybrid airfoils were normalized by C_0, so a standard hinge location was set at 0.25 x/C_0 for hybrid designs with scale factor of 3.

The TUNDROP code[20] is a modification to the AIRDROP code that analyzes the airfoil in the presence of wind tunnel walls. This code generates a potential flowfield with additional panels modeling the upper and lower walls of the two-dimensional tunnel. The code then calculates droplet trajectories based on the flowfield with walls present and provides the collection efficiency on the surface. TUNDROP also gives C_P data for the surface of the airfoil, as well as a normalized change in velocity ($\Delta U/U_\infty$) on the airfoil surface and the tunnel walls, which can be used to compare the wall effects. TUNDROP results were used to evaluate the effects of the tunnel walls on the hybrid solution.

2. *Alternative Hybrid Designs*

The cambered hybrid design method led to accurate ice shapes at a single design angle of attack, α_D. For multipoint designs over a range of angles of attack, flaps were added. The symmetric flapped hybrid design is an alternative design method that can be employed. The symmetric, flapped design is the predecessor to the cambered hybrid design and was successfully tested by NACA in the 1950s.[3] An example of this design is shown in Fig 2.4 with a cambered design. The flapped hybrid airfoil design is created by merging the full-scale leading-edge section with a near-symmetric aft body. The symmetric body was created in PROFOIL by setting C_{m0} and nose droop equal to zero. A flap is added to the design, with the hinge set at 25% x/c_0, in order to adjust the circulation of the airfoil to match the full-scale ice accretion over a range of angles of attack. This method may be advantageous in model construction due to its simplicity, while providing a model that performs well over a range of angles of attack. At high angles of attack, the simple flap may cause flow separation, which could be improved by more advanced flap designs in the future.

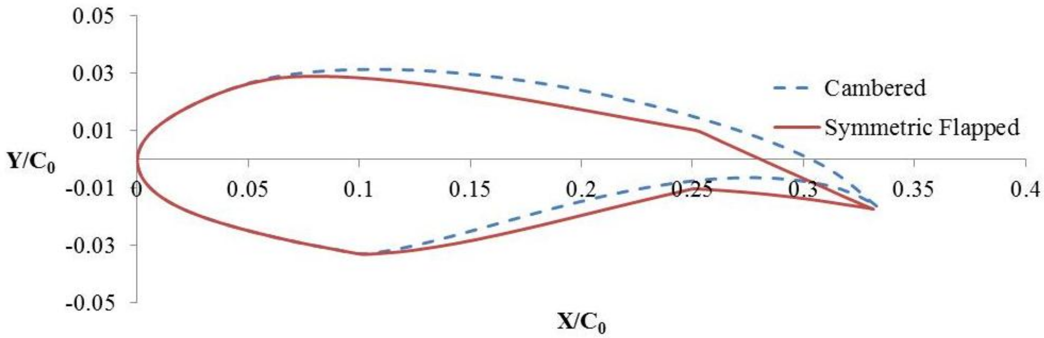

Fig. 2.4 90% span symmetric flapped hybrid (Δf=12°) and cambered hybrid (α_D=4°) designs.

3. *Hybrid Airfoil Analysis*

Determining the accuracy of a hybrid model design required a thorough comparison of the ice accretion on the candidate hybrid design and full-scale airfoil. There is a list of parameters that can be used to examine the ice accretion and aerodynamic characteristics of the airfoils; the C_P plots, including the stagnation point and suction peak, airfoil circulation (through lift coefficient), droplet collection efficiency, and the LEWICE predicted ice shape. Comparing these parameters gave a measure of the accuracy of the hybrid design method.

Flowfield characteristics, such as the C_P distribution and circulation, are representative of the airfoil flowfield that influence both droplet impingement and ice-shape growth. The airfoil circulation controls the curvature and path of the streamlines and particles as they encounter the airfoil, which is especially important for small droplets, which are more sensitive to the flow. Generally the hybrid designs require a lower circulation than the full scale to achieve matched ice shapes, but the reduction in circulation is not a known parameter.[4] The C_P plots, which are directly related to surface velocity on the leading edge help to determine the heat-transfer characteristics of the droplets and water on the airfoil's surface. The example C_P plot in Fig. 2.5 shows the C_p distribution is nearly matched in the leading-edge of the hybrid design. The location of the stagnation point and suction peak on the leading edge of the airfoil as well as the suction peak C_P are often used as indication of the leading-edge flowfield.

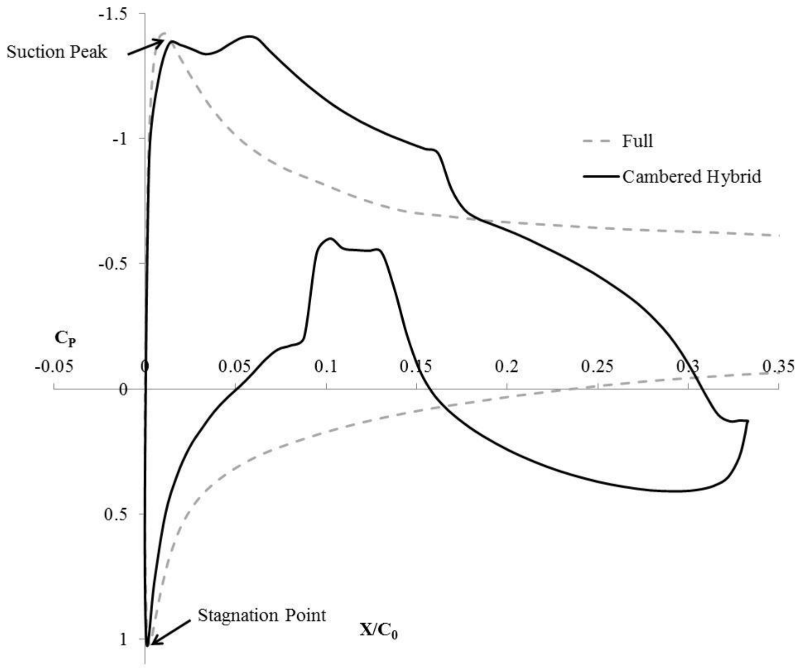

Fig. 2.5 Example Cp plot for a hybrid airfoil (60%, α_D=2°)

Direct comparison of calculated icing parameters is also useful in the evaluation of the hybrid design. The β curve is generated by AIRDROP in the execution of the hybrid design method, and by LEWICE in the calculation of the ice shape. A β curve can also be created with tunnel walls using the TUNDROP program. The sample β curve, shown in Fig. 2.6, gives the upper and lower impingement limits, as well as the maximum impingement location. As the ice shape grows as predicted by LEWICE, the β curve usually narrows with the changing geometry. Full-scale and hybrid ice shapes generated by LEWICE are very useful in evaluating the hybrid design at each angle of attack. These ice shapes are generated by defining the free-stream velocity, median droplet diameter, airfoil chord, liquid water content and temperature. There are six parameters usually used to describe ice shapes; three are shown on the ice shape in Fig. 2.7.[21] Horn length, horn angle, and maximum thickness describe the size of the ice horn that forms on some ice shapes, and is often indicative of the effect of the ice on aerodynamics. The other three variables (stagnation thickness, impingement length, and maximum width) help to define the ice shape.

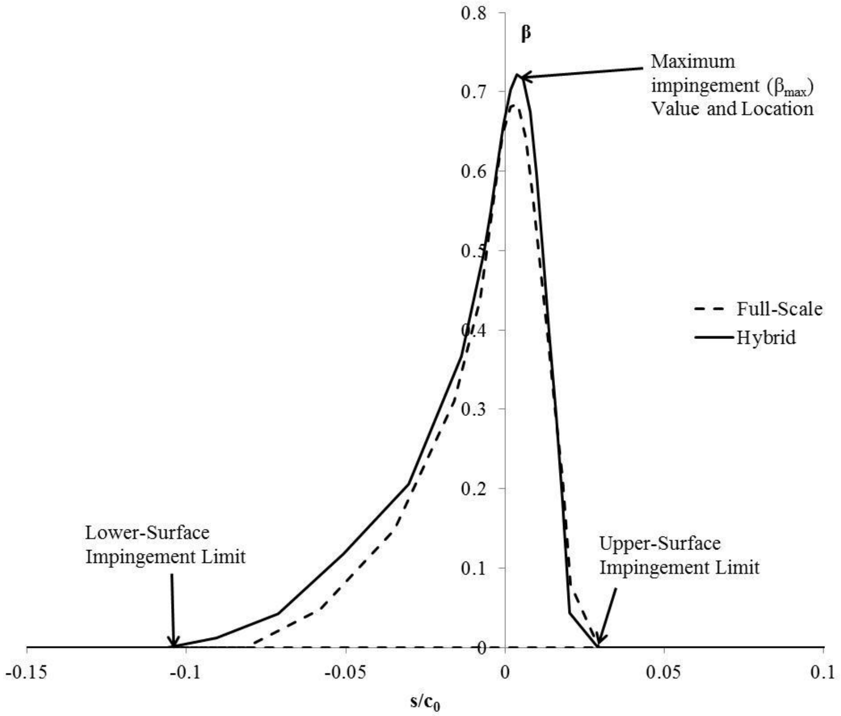

Fig. 2.6 Example β distribution (60% span, α_D=2°).

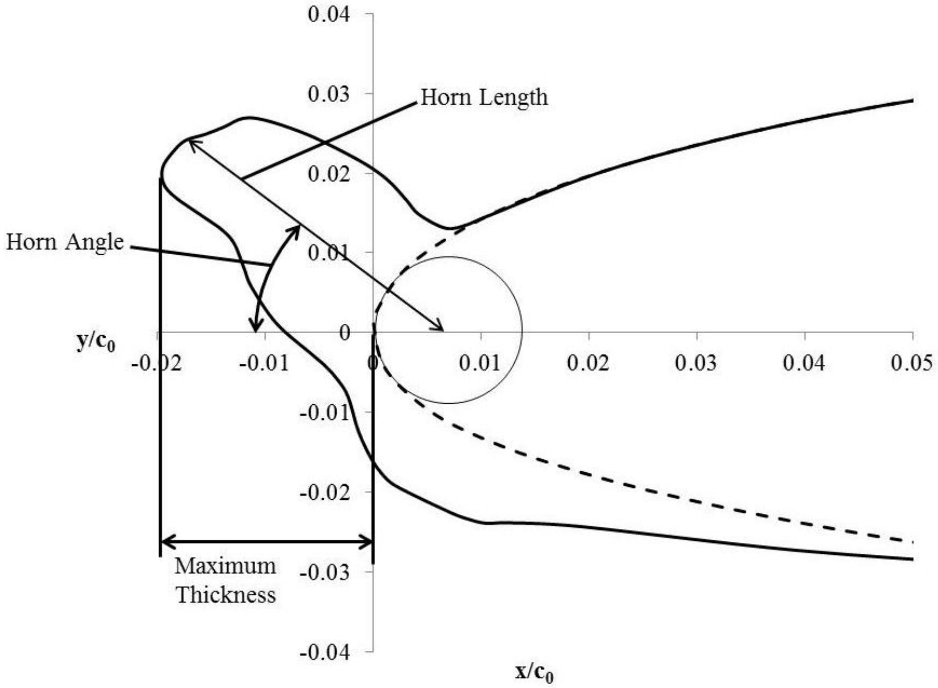

Fig. 2.7 Example ice shape with labeled characterization parameters (60% span, α_D=2°).

III. Results and Discussion

To complete a systematic evaluation of the hybrid design method for large-scale swept wings, an initial design was optimized at a baseline design point. From that baseline design, trade studies were used to determine the effects of varying the hybrid scale factor and leading-edge extents. Then designs are compared for different spanwise sections of the hybrid airfoil, and for different full-scale angles of attack. Based on these comparisons, the effects of flowfield parameters, such as the stagnation point and circulation, were evaluated for their effects on ice shape. Finally, the effects of tunnel walls were evaluated to determine how they affected the design. A short evaluation of tunnel wall corrections was also performed to determine if applying corrections to the design is valuable.

A. **Initial Baseline Hybrid Design**

The creation of a baseline hybrid design for this study began in the selection of a spanwise section. The 60% span airfoil was selected because it was far away from discontinuities in the planform while maintaining a fairly large ice shape as normalized by the chord. The baseline free-stream icing conditions selected for this study are a temperature of 20°F (-6.7°C) and median droplet diameter of 40μm. These conditions were selected because they lead to horn ice formation on this airfoil for icing times over 10 minutes and provided a large chordwise extent of the ice shape. The liquid water content was set at 0.5 and tunnel speed of 229 mph to match conditions set for the NASA project. These free-stream conditions will be referred to as the baseline icing conditions. The CRM65 chord is 10.1 feet at 60% span. In the NASA Icing Research Tunnel, the tunnel height to airfoil chord ratio (h/c) is 0.9 for an airfoil mounted vertically. The evaluation of wind tunnel effects by Bragg and Wells[14] showed reduced effects of tunnel walls as h/c increased above 2. A hybrid scale factor (SF) of 3 was selected to create a reasonably sized model without reducing the chord far enough to compromise the accuracy of the model. The impingement limits for this airfoil at $\alpha = 2°$ and the baseline conditions were about $x/c_0 = 0.07$ on the lower surface and $x/c_0 = 0.03$ on the upper surface. This led to the selection of leading-edge chordwise extents of 10% on the lower surface and 5% on the upper surface. The initial hybrid design for the baseline case had a nose droop of 2° down and $c_{m0} = -0.18$, and is presented in Fig 3.1.

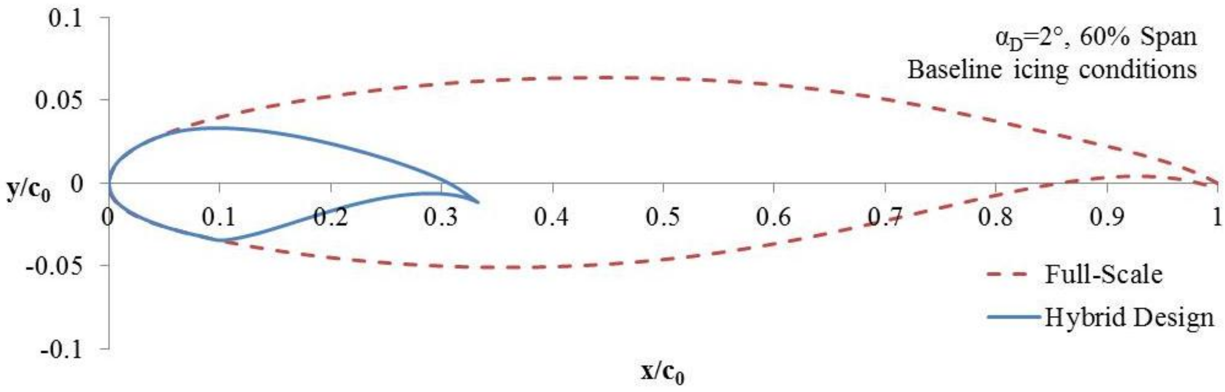

Fig. 3.1 Initial baseline hybrid design compared to the full-scale airfoil.

B. **Studies of Hybrid Design Parameters**

The design of a hybrid airfoil requires the selection of three geometric parameters, the hybrid scale factor and upper and lower surface leading-edge extents, as well as the iteration of two design parameters to match the β curve, the nose droop and c_{m0}. First a sensitivity study was performed to determine the effects of small variations of nose droop and c_{m0} on the hybrid design. Then designs were made varying the leading-edge extents of the design to determine the effect on ice shape accuracy. Finally, airfoils were designed at different hybrid scale factors, to determine the ice shape accuracy of designs at high scale factors.

1. *Sensitivity study of Hybrid Design Parameters*

Arriving at an accurate hybrid design required iteration of the hybrid design parameters of nose droop, and C_{m0}. While the selection of these parameters affects the accuracy of the model, there are also inaccuracies inherit to LEWICE simulations. The nose droop is an angle defined as the angle between the chord of the maintained full-scale leading edge and the hybrid airfoil chord from leading to trailing edge. The hybrid airfoil angle of attack is set so that the leading edge matches that of the full scale, so the effective angle of attack, for the leading to trailing edge hybrid chord is increased as the nose droop angle increases.[7] The nose droop for the designs in this research was iterated to converge to within ±0.1°, so to determine the sensitivity of the nose droop parameter, the parameter was increased and decreased in this study by 0.5 and 1°, while keeping C_{m0}, α, and SF constant. The resulting designs are shown in Fig 3.2, along with the change in the predicted LEWICE ice shape.

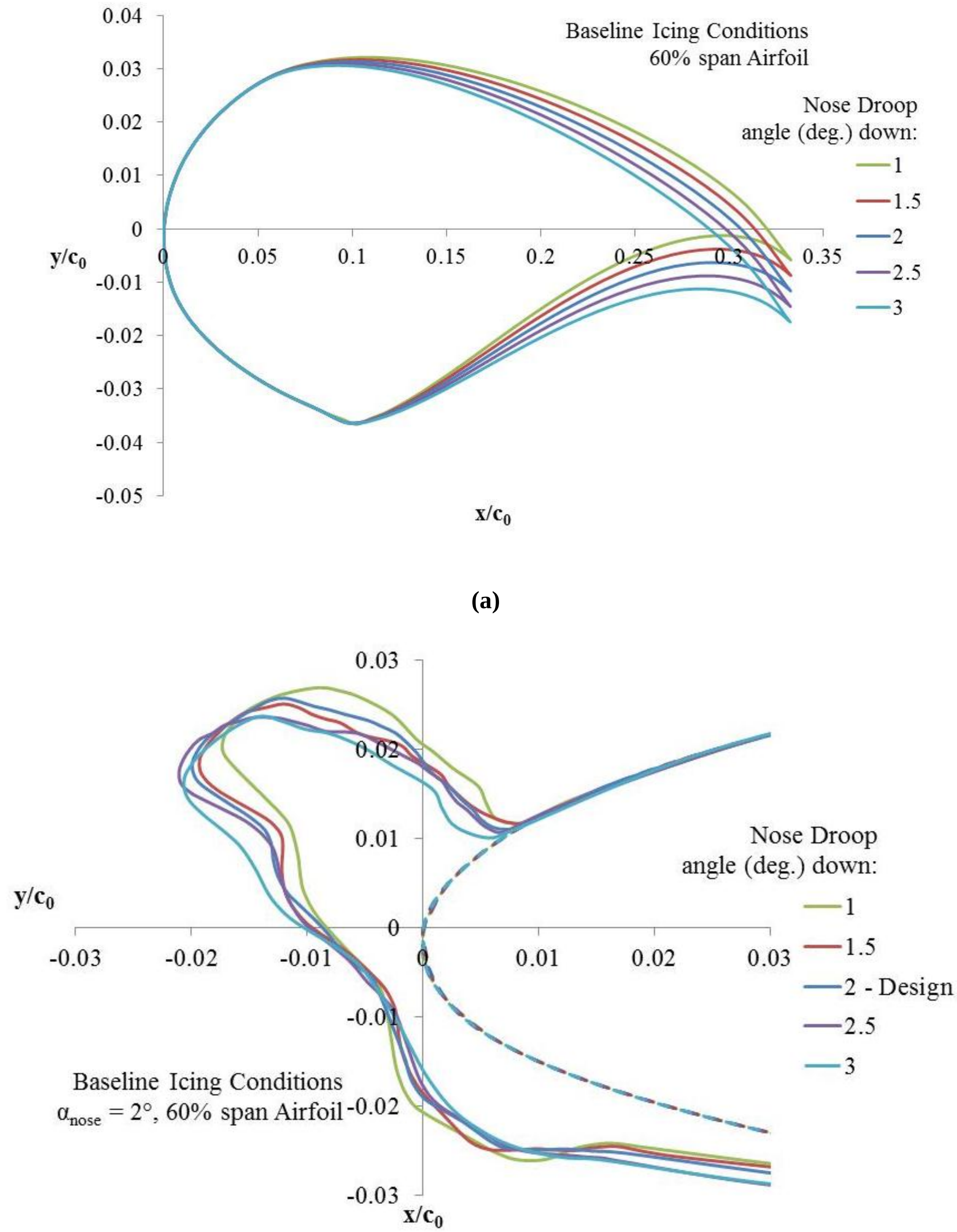

(a)

(b)

Fig. 3.2 Sensitivity analysis for changing nose droop on the (a) hybrid airfoil design and (b) LEWICE predicted ice shape.

Adjusting the nose drop changes the camber of the hybrid airfoil while maintaining the leading edge geometry. As the nose droop increases, the circulation increases, and the ice horn moves down the leading edge of the airfoil. The nose angle of attack is held constant; however, the effective angle of attack, defined from the leading to trailing edge chord, increases with increasing nose droop. The 1° shift in nose droop is leads to a small shift in the ice horn angle. While a change in nose droop leads to small changes in final ice shape, as the nose droop increases downward, there is a decrease in the aft loading.

Changing the C_{m0} of the hybrid design adjusts the amount of camber in the hybrid airfoil while maintaining the leading and trailing-edge positions. As the value becomes more negative, for the same angle of attack, the circulation and lift coefficient increase. The values of c_{m0} were iterated to converge within ±0.01. The values of C_{m0} were adjusted by 0.05 in each direction to determine the effect on the model design and ice shape. The airfoils and LEWICE predicted ice shapes are in Fig. 3.3. There is a small change in the ice shape between -0.13 and -0.18, but a much more significant change between -0.18 and -0.23. Nose droop and C_{m0} adjust the camber and circulation of the hybrid airfoil. Nose droop changes the effective angle of attack by moving the trailing edge while keeping the nose constant. C_{m0} increases the circulation by increasing the camber of the designed aft section while maintaining the leading and trailing edge point. An airfoil with high nose droop risks separation on the upper surface, while an airfoil with high C_{m0} risks separation on the lower surface at the leading-edge extent. The separation risk is due to an increase in the adverse pressure gradients seen in the C_P plots in Fig. 3.4. Figure 3.5 compares the two variations in hybrid design with x/c_0 and y/c_0 at the same scale. The effects of these variables are not linear, so careful attention is needed in setting these variables to match the full scale ice shape.

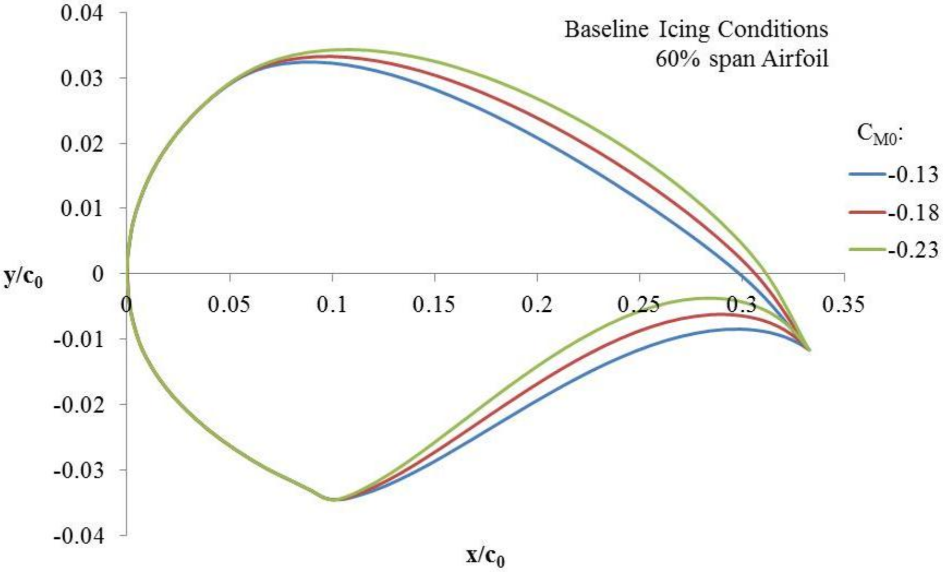

(a)

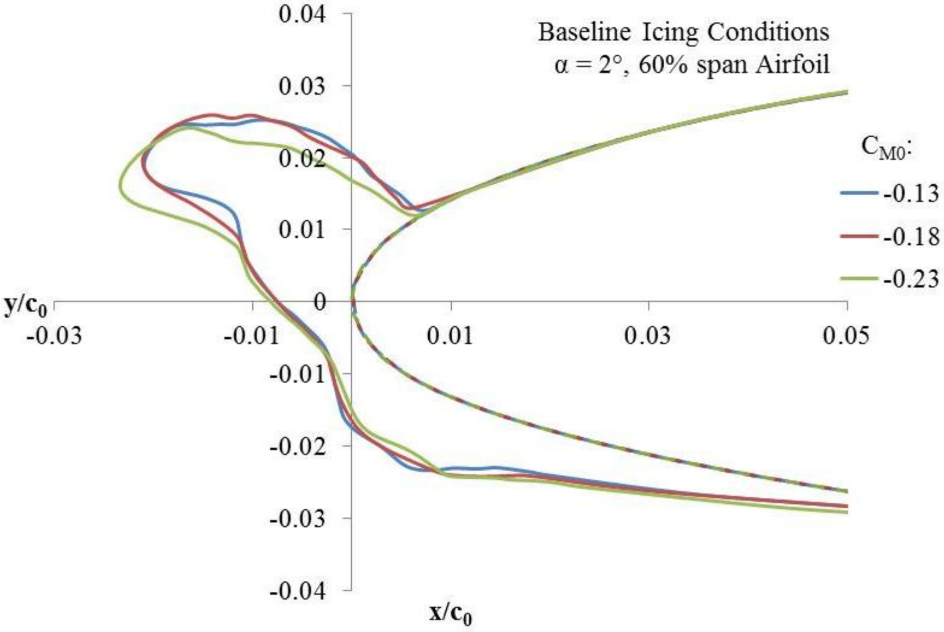

(b)

Fig. 3.3 Effect of change in C_{m0} on (a) hybrid airfoil shape and (b) LEWICE predicted ice shapes.

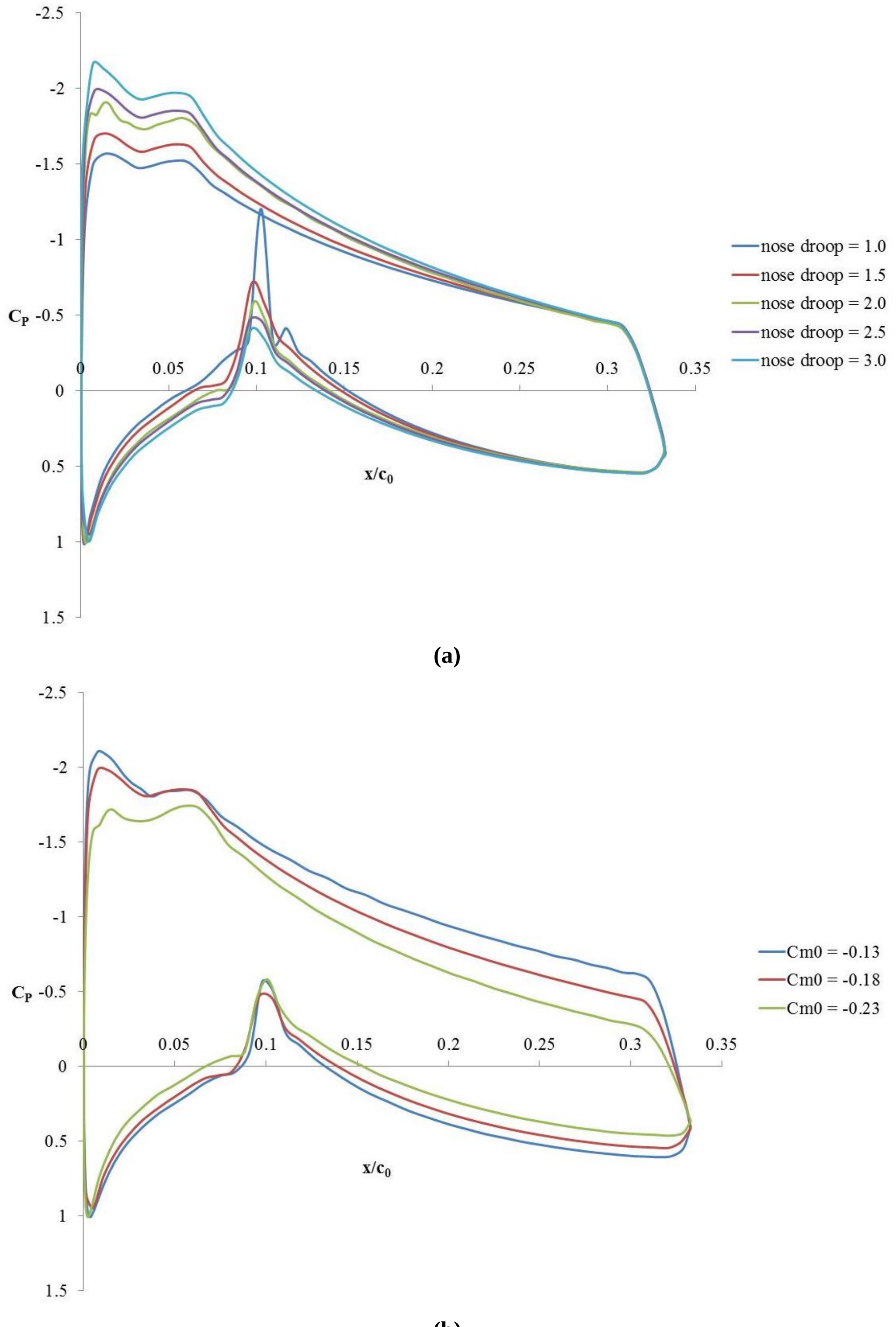

(a)

(b)

Fig. 3.4 C_P plots for variation in (a) nose droop and (b) C_{m0}.

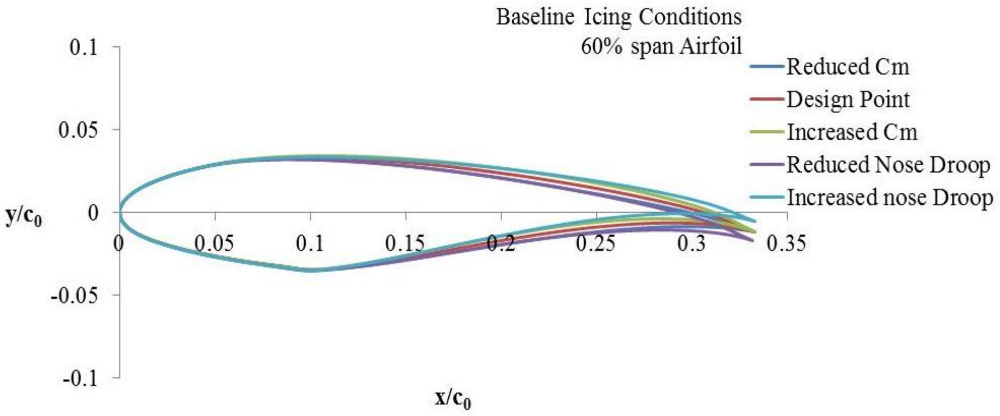

Fig. 3.5 Adjustments to nose droop and zero lift moment coefficient on airfoils with equal x/c and y/c scales.

2. *Leading-Edge Chordwise Extent*

Selecting the location for the upper-surface and lower-surface leading-edge extents is primarily dependent on the location of the droplet impingement limits. The leading-edge extent is the x/c_0 location where the full-scale leading edge transitions into the hybrid airfoil aft section. Generally this point is selected to lie slightly behind the calculated impingement limits on the upper and lower surface of the full-scale airfoil. Considerations for icing protection systems and runback ice can also set limits on the minimum leading-edge extent. Larger leading-edge extents, especially on the lower surface, limit the aerodynamic design of the aft section of the airfoil.

Four values of the lower-surface leading-edge extent were compared to determine the change in performance of the hybrid design. The CRM65 wing 60% span section was designed with SF = 3 and leading-edge extents of 3, 5, 10, and 15% on the lower surface, as shown in Fig. 3.6. The upper-surface extent was set to 5% for the hybrid designs with lower extents at 10, and 15%. The upper-surface extents were reduced to 3% for the design with a 3 and 5% lower-surface extent. For all four designs nose droop, C_{m0}, and α_D are held constant. The upper-surface extent had less of an effect on the performance of the hybrid airfoil, because the lower surface ice accretion extends farther back on the lower surface.

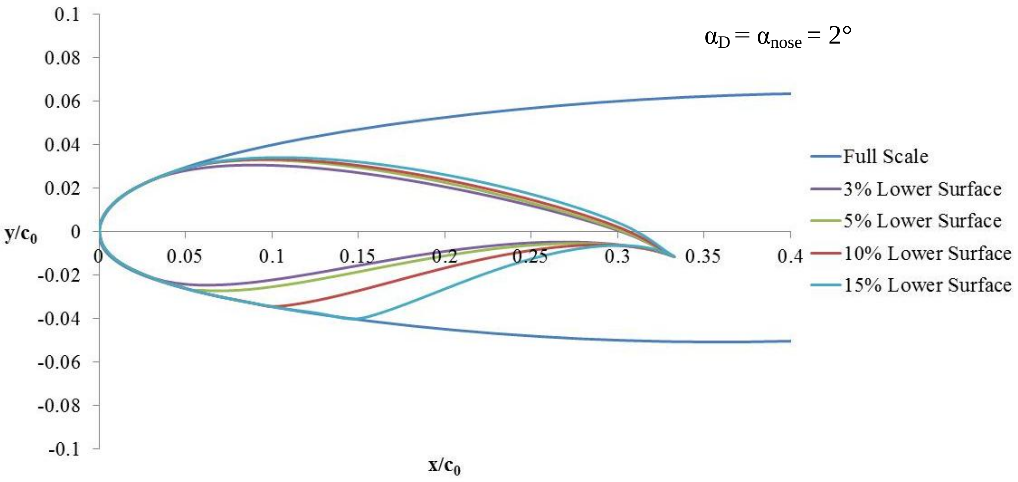

Fig. 3.6 Hybrid airfoils with varied lower-surface leading-edge extents.

The full-scale ice-accretion limits, determined from the initial limits of impingement in normalized surface coordinates for the standard icing conditions at $\alpha_D = 2°$, are 10.6% on the lower surface and 2.1% on the upper surface. The 10 and 15% leading-edge extents maintain the leading edge over the entire accretion region. The 3 and 5% extents occur before the lower-surface accretion limit, which affects the tail of the droplet impingement curve. The upper surface ice horn remains largely unchanged by the change in lower-surface extents; however, in the designs where the lower-surface extent occurs before the ice-accretion limit, a small second horn forms below the stagnation point, as can be seen in Fig. 3.7. To prevent this error, the leading-edge extents should be downstream of any ice accretion limits. All hybrid ice shapes predicted in LEWICE overpredicted the ice horn length as compared to the full-scale shapes. This overprediction was also seen in the collection efficiency, shown in Fig. 3.8, as an increase in β_{max}. The limits of impingement shown on the β curves change with the leading edge extents, decreasing for the 5% and 3% lower surface leading-edge extent cases.

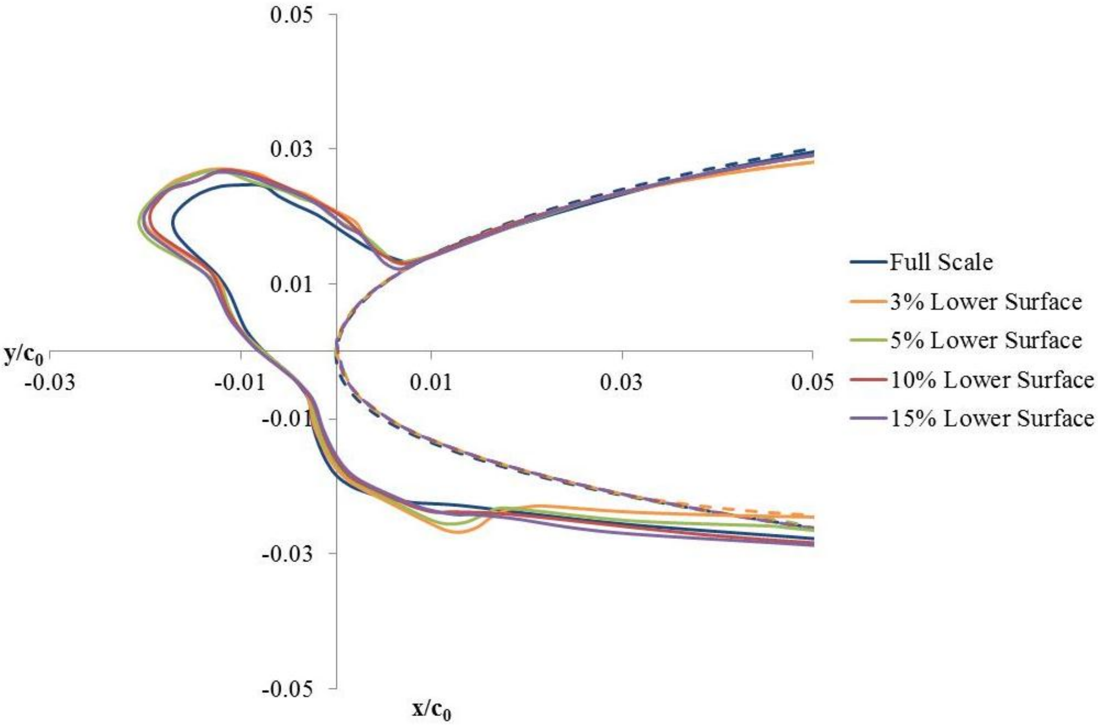

Figure 3.7 Ice shapes for lower surface leading-edge extents varied from 3% to 15% full-scale chord.

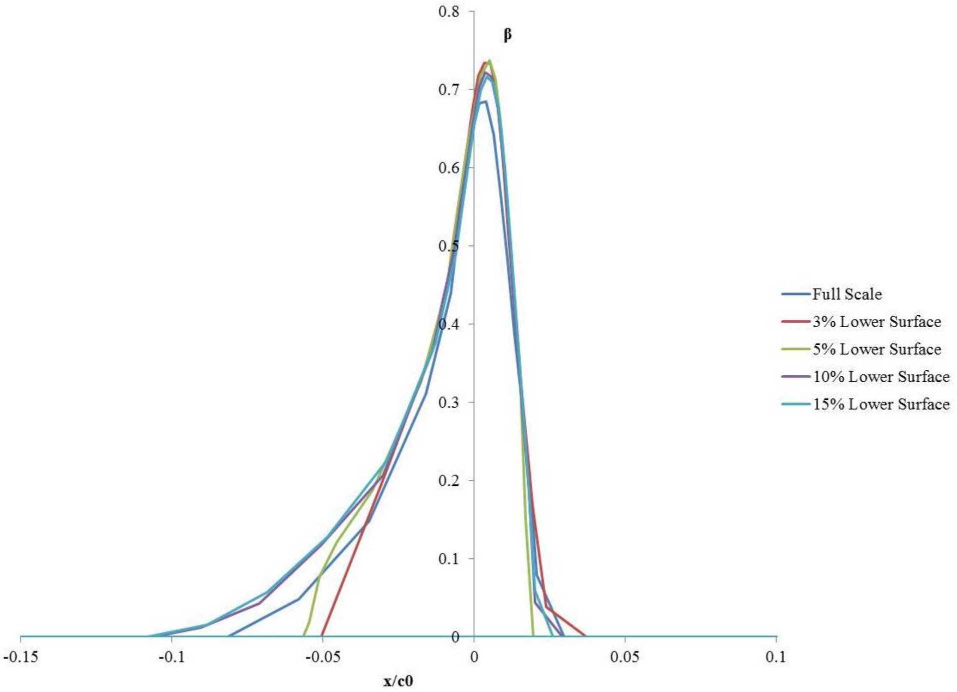

Fig. 3.8 Droplet impingement curves for variation in lower surface leading-edge extent.

Moving the lower-surface extents farther downstream may also cause problems with separation on the hybrid design. As the lower-surface leading-edge extent increases, the suction peak created on the lower surface increases as well as seen in Fig. 3.9. This increase is caused by the increase in second derivative of the surface at the junction of the leading-edge and aft sections on the lower surface of the hybrid design where the aft section has been redesigned to increase camber and achieve higher circulation. The leading-edge extents couple with SF to increase the lower-surface suction peak and the potential for separation. On an airfoil with SF of 2, a 15% leading-edge extent comprises 30% of the hybrid airfoil. For the hybrid airfoil with SF of 5, the same 15% leading edge extent covers 75% of the hybrid airfoil. Fig. 3.9 shows the increasing lower-surface suction peak as a function of the leading edge extent for the CRM65 60% span airfoil, which could lead to separation on the lower surface. The change seen in upper surface C_P may be due to the change in upper surface leading-edge extent which is 3% for the 3 and 5% lower surface extents, and 5% for the 10 and 15% lower surface extents.

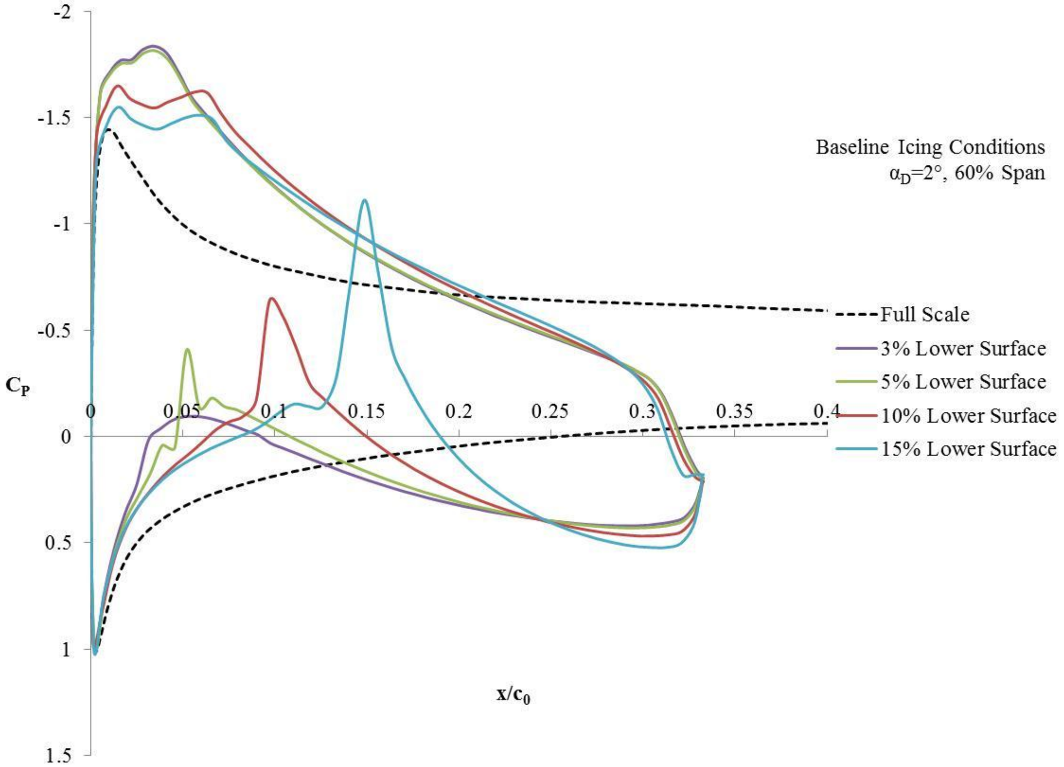

Fig. 3.9 C_P distributions for 60% span CRM 65 airfoil with varying lower-surface leading-edge extents.

3. *Hybrid Scale Factor (SF)*

The length of the hybrid chord was determined by the hybrid scaling factor, SF, which is defined as the full-scale chord over the hybrid chord. Initially the hybrid design was tested up to an SF of 2,[17] but any SF greater than one can be considered. The maximum hybrid model chord was determined by acceptable wind tunnel blockage or model construction considerations. As the SF increases, proper design of the aft section becomes more challenging because of the limits of the full-scale leading edge. To study the effect of SF, airfoils with SF = 2, 3, 4, and 5, shown in Fig. 3.10, were created from the 60% span CRM65 airfoil. The hybrid designs were tested to determine the effects on ice shape accuracy and evaluate the probability of flow separation. Input variables for each design are included with appendix B. As the hybrid scale factor increased, the design required a more negative c_{m0} and less nose droop to accurately match the impingement curve. For the SF = 4 and 5 designs, the lower surface leading- edge extent was reduced from the baseline 10% to 5% to accommodate the increased C_{m0} and shortened chord. Wind tunnel blockage estimates for the Icing Research Tunnel will also be compared, and a more complete discussion of blockage will be included later with the discussion of tunnel wall effects.

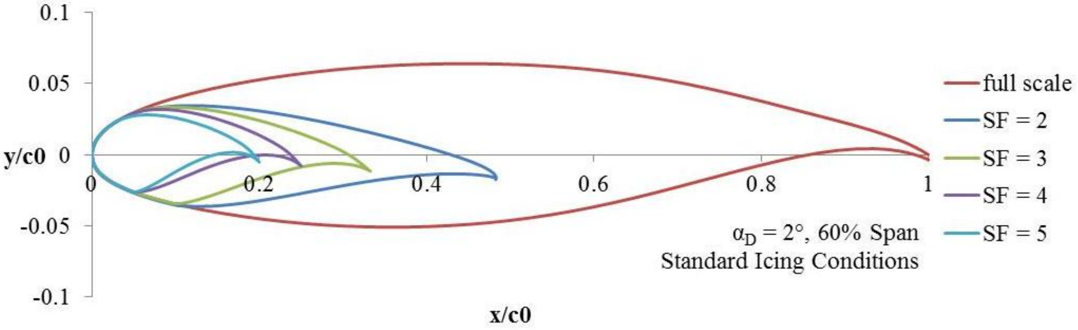

Fig. 3.10 Hybrid airfoils with varied hybrid scaling factors.

The ice shapes and β distributions for each hybrid design are presented in Figs. 3.11 and 3.12, respectively. Over this range, there was not a significant reduction in accuracy of the ice-shape simulation with increasing scale factor. Error in horn length did not exceed 12% and horn angle changed by less than 8° for all designs. The β distributions showed a slight increase in maximum collection efficiency, β_{max}, and a narrowing of limits of impingement with increasing scale factors which may be due to changing leading-edge extents. The increase in β_{max} is consistent for all of the hybrid designs, as is the over-prediction of ice shape horn length. There is also a steep drop seen in the β distributions for the SF 4 and SF 5 hybrid designs near 0.05 x/c_0 on the lower surface at the reduced leading-edge extent location. The reason for these changes to the collection efficiency may be a subject for further study, but they do not significantly affect the predicted ice shape.

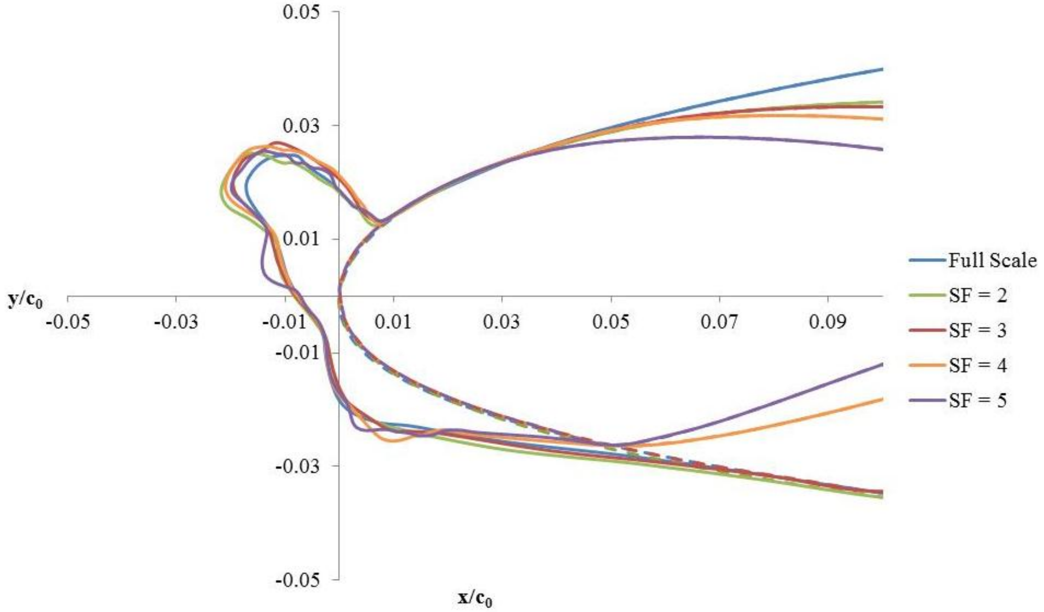

Fig. 3.11 Ice shapes for hybrid designs with varied scaling parameters.

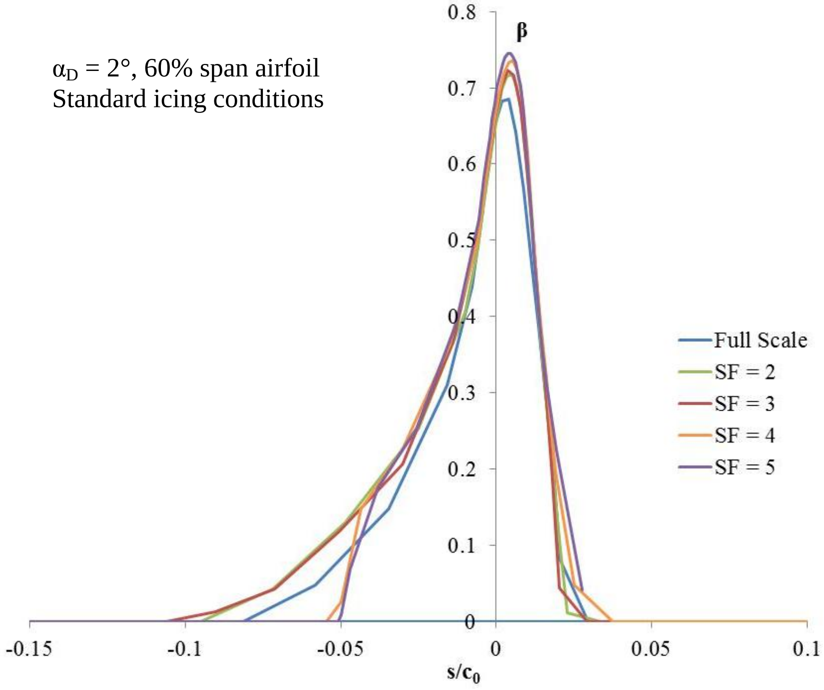

Fig. 3.12 Collection efficiency (β) for varied hybrid scaling parameters.

Increasing SF for a hybrid design significantly decreases wind tunnel blockage for an experiment. A more complete discussion on blockage will be presented later in this chapter. The height-to-chord ratio (h/c) increases from less than one for the full scale model to 4.5 for the SF 5 model when calculated for the Icing Research Tunnel test section compared to the CRM65 as defined in chapter 2. The height-to-chord ratio is the wind tunnel height, perpendicular to the chord, divided by the airfoil chord and is a measurement of the tunnel wall effect, with lower numbers indicating higher tunnel blockage. The effect of height-to-chord ratio on droplet impingement has been studied and shown that errors decrease with height to chord ratios over two.[22] Hybrid airfoils can experience high lift coefficients because for the same circulation the lift coefficient is multiplied by the SF. Figure 3.13 presents viscous C_P plots generated by XFOIL for the full scale, SF 3 design, and SF 5 design at α_D=2°. The stress on the aerodynamic design increases directly with increasing SF, which can lead to separation over the trailing edge or at the intersection of the full-scale leading edge and hybrid aft section. This effect is shown by the adverse pressure gradients in the C_P plots. In the SF 5 scaling trailing-edge separation is predicted, and in both hybrid models there is a suction peak in the lower surface at the intersection between the full-scale leading-edge and hybrid trailing-edge. This peak may lead to separation on the lower surface, decreasing the effectiveness of the hybrid design.

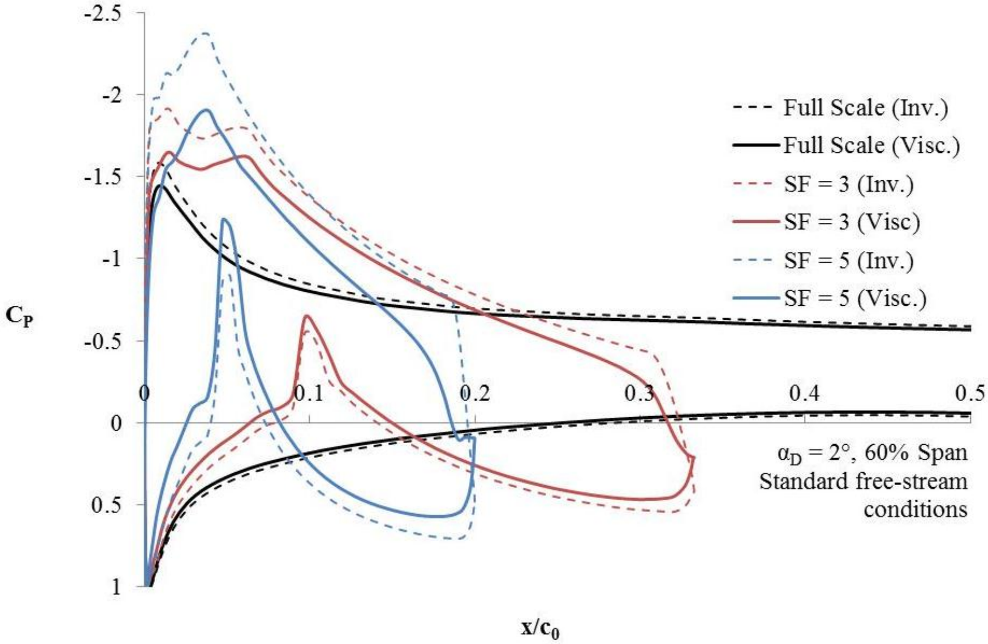

Fig. 3.13 Inviscid and viscous C_p plots for full scale airfoil and SF = 3 and SF = 5 hybrid airfoils at α_D=2°.

C. **Hybrid Design for Varied Conditions**

A standard design was selected as a baseline for the CRM 65 wing. When it is not otherwise stated in the following tests, the SF was selected to be three. This design sufficiently reduced tunnel blockage at all three selected CRM65 airfoil stations, but does not have as much risk of separation at high angles of attack. The scale factor of three also enabled the design to have larger leading-edge extents. The leading-edge extents for the airfoils are 5% on the upper surface and 10% on the lower surface unless otherwise stated. This design provides acceptable ice-shape accuracy for the $\alpha = 2°$ case under the baseline icing conditions; however, as the conditions change, the design variables may need to change as well.

1. *Variation in Full-Scale Chord*

In order to produce airfoils that are well conditioned for wind tunnel testing, the hybrid design of a highly tapered wing, such as the CRM65, required airfoils of different chords to be considered. As the full-scale chord changes, the droplet inertia parameter changes, which affects droplet impingement limits. As the airfoil gets smaller, the impingement limits increase. When the airfoil chord increases, the limits decrease, but the tunnel blockage increases. The chord of the airfoil plays a role in the selection of the SF and impingement limits of the design.

The three spanwise sections from the CRM 65 each had different chords and characteristics. The 60% span CRM airfoil had a chord of 10.1 feet, which is a height to chord ratio of 0.9 in the Icing Research Tunnel. Since a height to chord ratio above 2 is desirable for high-quality aerodynamic testing as discussed previously, a hybrid scale factor between 2.5 and 4 would be needed. Figure 3.14 shows the 60% airfoil and hybrid design with scale factor of 3. This full-scale airfoil has a supercritical design, which increases the aft loading and circulation at a given angle of attack. This results in a slightly higher C_{m0} in the hybrid design. The airfoil thickness is also an important consideration in the design because thicker airfoils have a tendency to experience trailing-edge separation. The scaled thickness value of the hybrid will often be much more than the original full-scale airfoil. The thickness of this 60% span CRM airfoil is 11.4%, and the thickness of the hybrid airfoil design is 20.4%.

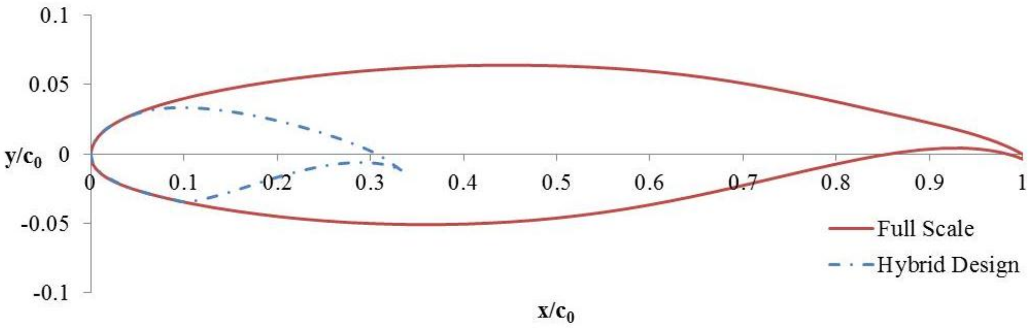

Fig. 3.14 60% span CRM airfoil and hybrid design.

Designing the inboard airfoil presents a more challenging case due to the larger size. Larger airfoils create more blockage in tunnel tests which requires a higher SF; however, the ice accretion limits are smaller, requiring shorter leading-edge extents. The full-scale chord of the CRM65 at 22% span is 19.7 feet, which gives a height to chord ratio of 0.45 in the Icing Research Tunnel. To bring this airfoil to a manageable length a hybrid scale factor of 4 is desirable. The ice accretion limits for this section were smaller than those of 60% span section, so the leading-edge extents are reduced. The 22% CRM airfoil is shown in Fig. 3.15 with a hybrid design that uses the same scale factor and leading-edge extents of the 60% cut as well as an alternative SF = 4 design that takes advantage of the change in impingement limits. Generated ice shapes and impingement curves for the 22% airfoil and both hybrid designs are presented in Fig. 3.16. The inboard section had less camber, generating less full-scale circulation, so the design values of C_{m0} and nose droop can be reduced for a given design.

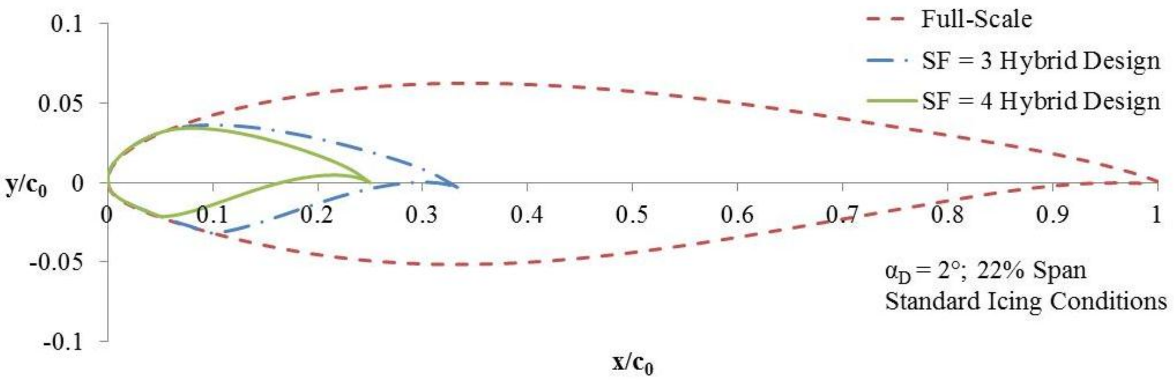

Fig. 3.15 22% Span CRM and hybrid airfoils.

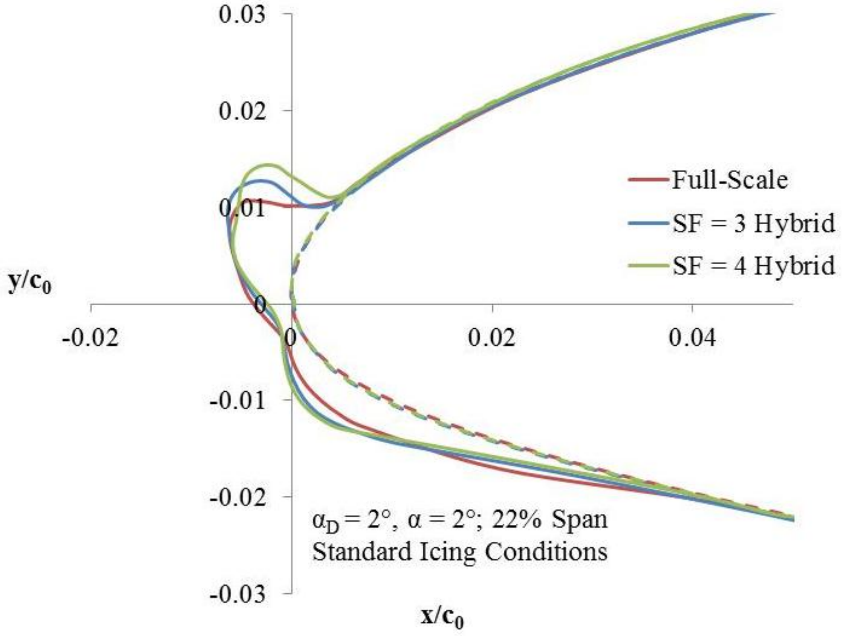

(a)

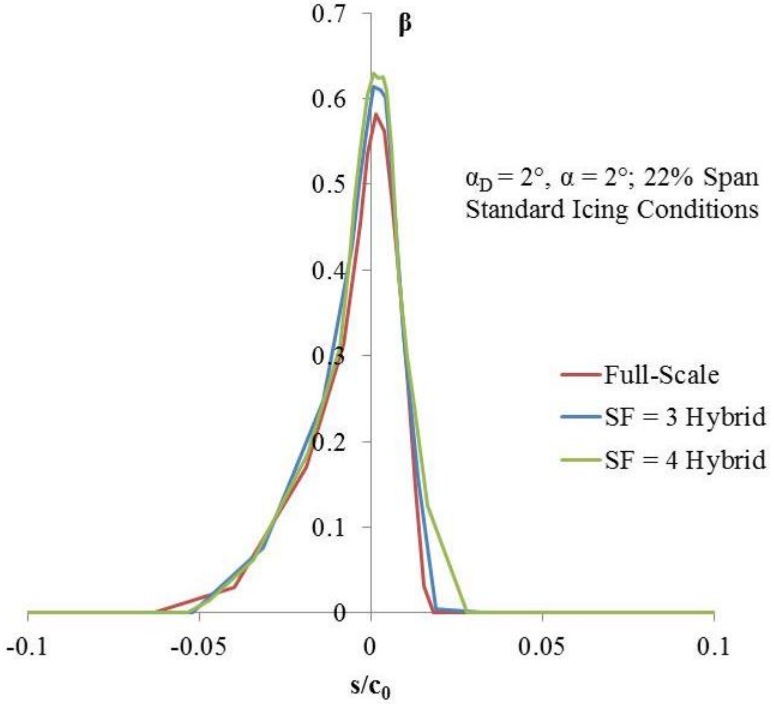

(b)

Fig. 3.16 (a) ice shape and (b) collection efficiency for the 22% span CRM full scale and hybrid.

As shown in the β distribution, β_{max} was slightly higher for the each of the hybrid designs, but appeared to match the full scale well over the rest of the airfoil surface. This increase in collection efficiency was consistent with a slightly larger ice horn on the hybrid airfoils, but the horn angle of the ice shape remained similar, increasing by less than 10° from the full-scale design to the SF = 4 design. The SF = 4 design provides an accurate ice shape while reducing the wind tunnel blockage. The higher scale factor designs offered a lower blockage option for airfoils that require smaller leading-edge extents and lower circulation.

The outboard airfoils were much smaller; the CRM65's 90% span airfoil has a chord of 6.1 feet, which meant that only SF of 2 was required. This lower scale factor allowed for more freedom in the hybrid design variables. The 90% span airfoil was plotted in Fig. 3.17 with a hybrid design with a scale factor of 3, matching the 10% lower surface leading-edge extents of the standard design, and a hybrid design with scale factor of 2, with leading edge extents selected to be at 15% x/c_0 . The lower droplet impingement limit was nearly 0.17 s/c_0 for the standard icing conditions on this airfoil, which was covered by the 15% lower surface leading-edge extent selected. Smaller airfoils produce larger ice accretions as normalized by airfoil chord, but reducing the scale factor allowed for larger leading-edge extents.

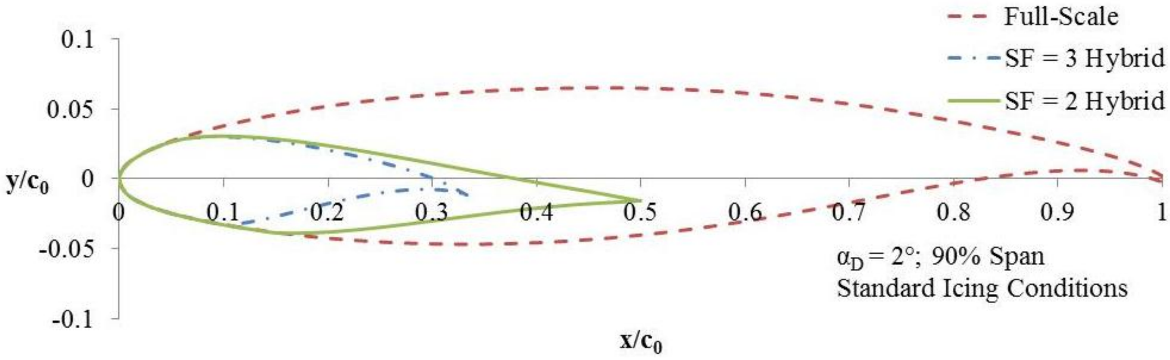

Fig 3.17 90% span CRM airfoil and hybrid designs.

The wing tip had more camber which requires a higher aft camber in the hybrid design, or C_{m0} value, to maintain the required airfoil circulation. A lower scale factor allowed the design to employ more nose droop and less aft camber to achieve the same circulation. Ice shape and beta distributions produced by these example wing-tip hybrid airfoils are shown in Fig. 3.18. With larger droplet impingement limits, the 10% leading edge extents were upstream of the lower surface impingement limit, which caused a small horn to form on the lower surface, as was shown earlier in Fig. 3.7. The lower scale factor allowed for 20% lower surface leading-edge extents, which removed the lower surface horn. The hybrid design matches the velocity distribution at the surface of the airfoil, so as the ice shape grows, the velocity may be less accurate and lead to divergence of the ice horn. The β distribution also had a slightly higher peak than the full scale but not as different as the inboard section. For airfoils of various chords, the SF and leading edge should be adjusted to accommodate the ice accretion limits and reduce wind tunnel blockage.

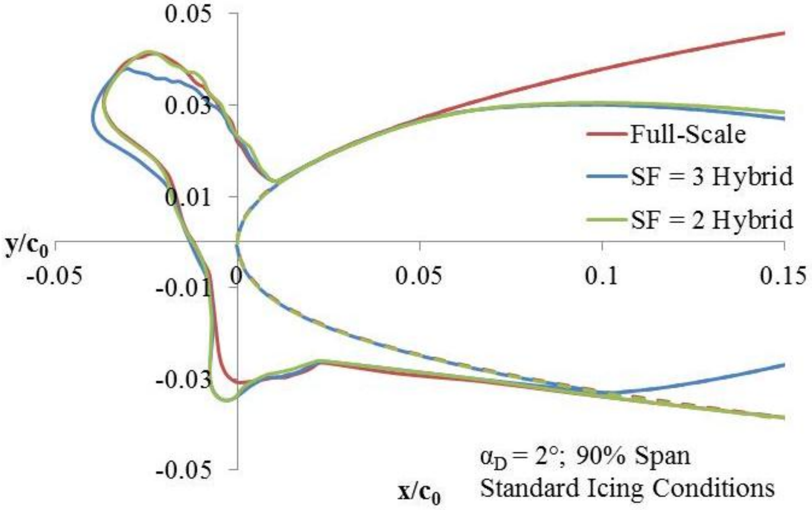

(a)

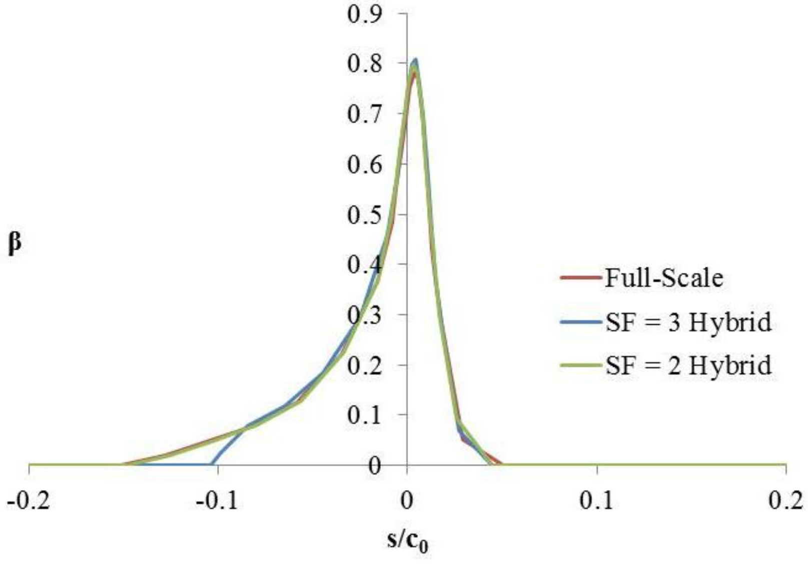

(b)

Fig 3.18 Comparison of the 90% span full-scale and hybrid airfoils of (a) ice shape and (b) β distributions.

2. *Variation in Angle of Attack*

A single element cambered hybrid airfoil design was specifically created for each angle of attack to be tested. As the full-scale angle of attack increases, the hybrid design must account for the increased circulation. This was achieved by increasing the aft camber and nose droop or by adding a flap to the design, to match the full scale β distribution and leading-edge C_P. For all angles of attack, the hybrid airfoil angle of attack was set so that the leading edge of the hybrid airfoil matches the leading edge of the full scale.[4] The chord line of the hybrid airfoil is defined for this research by the nose section chord as opposed to the line between the leading-edge and trailing-edge. The 60% span CRM airfoil hybrid designs for α_D= 0, 2, 4, and 6° are shown in Fig. 3.19. Each of the designs had an SF of 3, and lower-surface leading-edge extents of 10% chord. As defined earlier, the C_{m0} defines the aft camber of the hybrid airfoil, where the nose droop defines the intersection angle between the leading edge and the aft portion of the hybrid airfoil. Based on the sensitivity analysis presented earlier in this chapter, decreasing C_{m0} and nose droop together reduces the potential aft loading as opposed to a design that only adjusts C_{m0}. This helps reduce the probability of separation at the lower leading-edge extents. A design using more nose droop would have a high second derivative at the upper surface leading-edge extent which may lead to some separation as well. These four designs all provide a good approximation of the ice shape based on the LEWICE predicted shapes shown in Fig. 3.20.

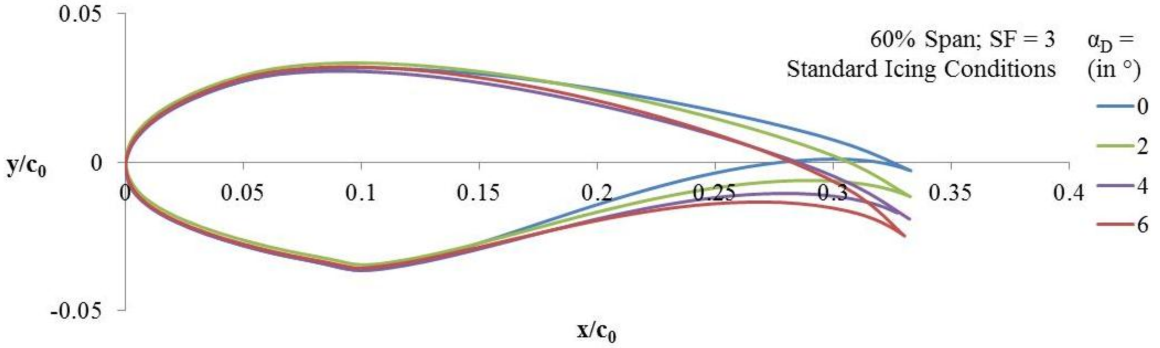

Fig. 3.19 Full-scale mid-span CRM airfoil and four hybrid designs for varied angles of attack.

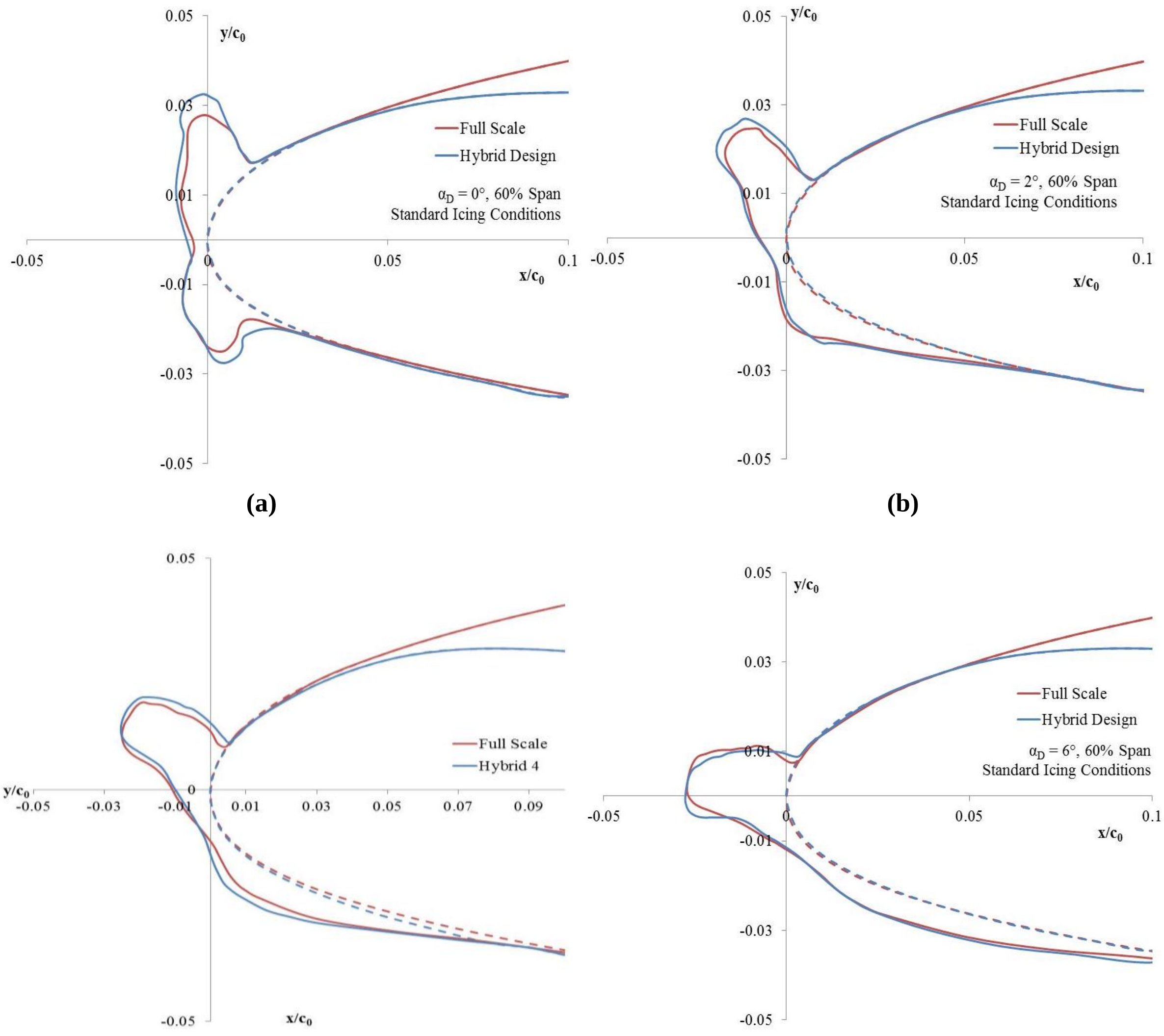

(a)

(b)

(c)

(d)

Fig. 3.20 Hybrid designs for (a) α_D=0°, (b) α_D=2°, (c) α_D=4°, and (d) α_D=6°.

3. *Circulation and Stagnation Point Matching*

Using the hybrid design during a wind tunnel test to match the full-scale ice shape requires an understanding of the icing conditions and the flowfield. At each angle of attack, changes in flap deflection or angle of attack may be required to optimize the hybrid airfoil simulation. Determining the correct angle for flap deflections can be accomplished through an understanding of how the performance of the hybrid design is affected by quantities such as circulation and stagnation point location. A better understanding of the relationship between these variables can also help when using hybrid designs with a flap to match the ice shape for off-design icing conditions.

The stagnation point location is representative of the flowfield and is the center of impingement in the limit as droplet size goes to zero. In theory, matching the full-scale and hybrid stagnations points and the leading edge geometry should match the flowfield around the leading edge. Circulation is also an important tool in evaluating the leading-edge flowfield. Prior tests of the hybrid design have shown that the circulation of the hybrid airfoil should be similar to, but less than that of, the full-scale.[8] If the circulation is assumed to be a vortex bound at the quarter chord, the vortex moves closer to the leading edge as the chord shrinks, and the influence on the leading-edge flowfield and droplet trajectories increase. Values of lift coefficient, non-dimensional circulation, suction peak, and stagnation point location are listed in Table 3.1 for the full scale airfoil over a range of angles of attack and hybrid designs which match the ice shape horn angle. The predicted ice shapes for these airfoils are all shown in either the study of hybrid scale factor, or design at varied angle of attack.

Table 3.1 Full Scale and Hybrid Design Flow-Field Variables

Airfoil	SF	α	Stagnation Point		C_l	$\bar{\Gamma} = \Gamma / u_\infty c_0$	Upper Surface C_P
			x/c_0	x (in)			$x/c_0=0.005$
60% Span	1	2	0.0027	0.3283	0.6470	0.3235	-1.3680
60% Span	2	2	0.0021	0.2554	0.8190	0.2048	-1.4690
60% Span	3	2	0.0016	0.1946	0.9910	0.1652	-1.3280
60% Span	4	2	0.0013	0.1581	1.0830	0.1354	-1.2440
60% Span	5	2	0.0009	0.1094	0.8860	0.0886	-1.0440
60% Span	1	4	0.0054	0.6566	0.8520	0.4260	-2.5810
60% Span	3	4	0.0044	0.5350	1.3400	0.2233	-2.4850
60% Span	1	6	0.0137	1.6659	1.0610	0.5305	-3.6460
60% Span	3	6	0.0080	0.9728	1.6020	0.2670	-4.2100

As the angle of attack increased for the full-scale design, the stagnation point moved farther back on the lower surface, the lift coefficient increased, and the upper surface C_P became more negative. In general, the nondimensional circulation decreased as SF increased. In prior studies, circulation decreased between 5 and 11% for SF = 2 designs depending on the aft design.[4] In this research, there was almost a 30% decrease in nondimensional circulation for the same design and a decrease of 73% for the SF = 5 design. Prior research has also indicated that there is a relationship between increasing scale factor and decreasing circulation.[4] The stagnation point for the hybrid designs were ahead of the full-scale stagnation points; however near the leading edge, it may be difficult to track small changes in stagnation point location. While stagnation point and circulation influence the flowfield, they are dependent on the aft section design and aft loading. Three hybrid designs for matched ice accretion under the same conditions are shown in Fig. 3.21, with C_P plots shown in Fig. 3.22. For each of the three designs, the overall circulation increased as C_{m0} becomes more negative and decreased as nose droop became more negative, but the leading edge flowfield and droplet impingement stays the same. The leading-edge C_P on the upper surface over the first 5% gave the best indication of ice shape match of the three parameters.

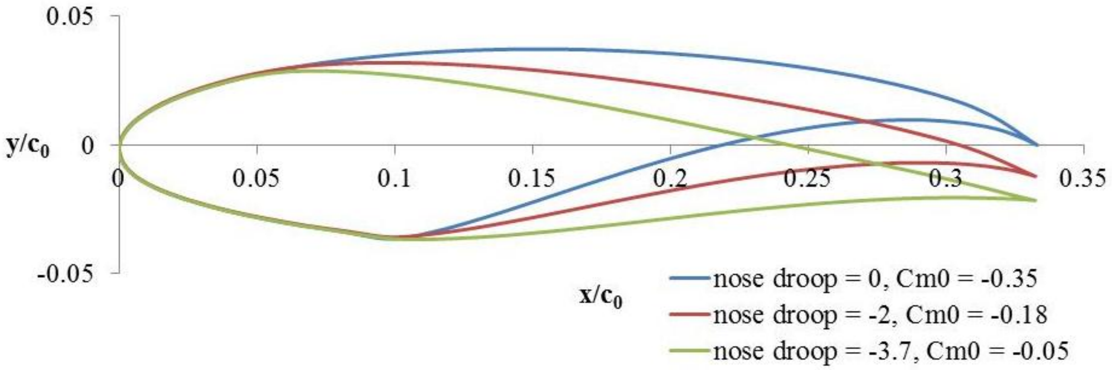

Fig. 3.21 Designs for $\alpha_D = 2°$, varied to match leading edge droplet impingement.

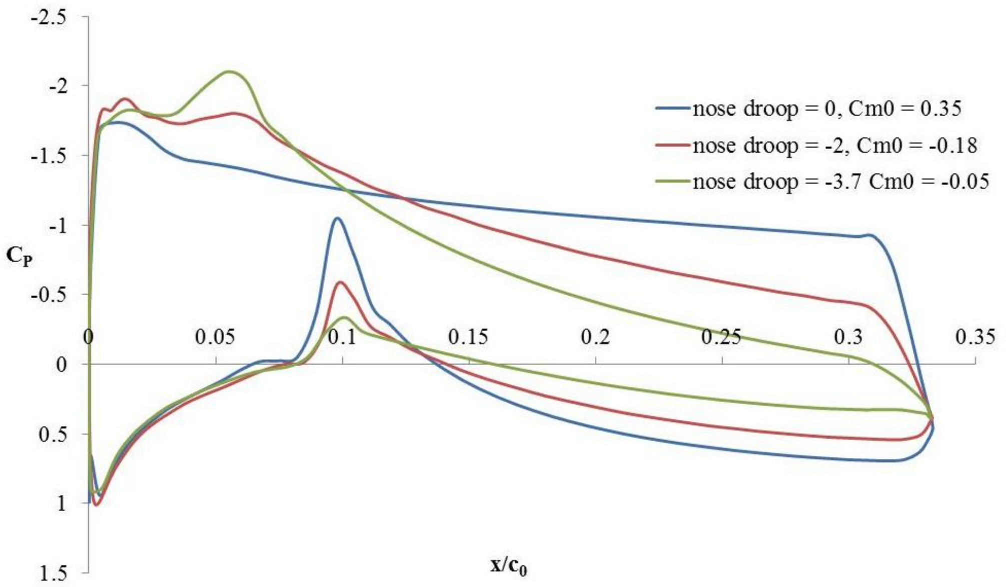

Fig. 3.22 C_P plots for the three designs at $\alpha = 2°$.

To match the stagnation point at $\alpha_D = 2°$, a flap was added to the last 20% of the baseline hybrid airfoil (SF = 3). After deflecting the flap 12° down, the stagnation point on the leading edge of the hybrid design matched the full-scale stagnation point. The stagnation point matched case predicts a horn angle that is too low, as can be seen from Fig. 3.23, where the LEWICE predicted ice shapes for the full-scale, standard hybrid design from the previous studies, and matched stagnation point hybrid are plotted. Matching the stagnation point generates higher circulation than the matched ice case, resulting in a lower ice horn. The droplet impingement curves are plotted in Fig. 3.24. For the stagnation point case, the curve is slightly shifted down, but maximum value remains nearly the same.

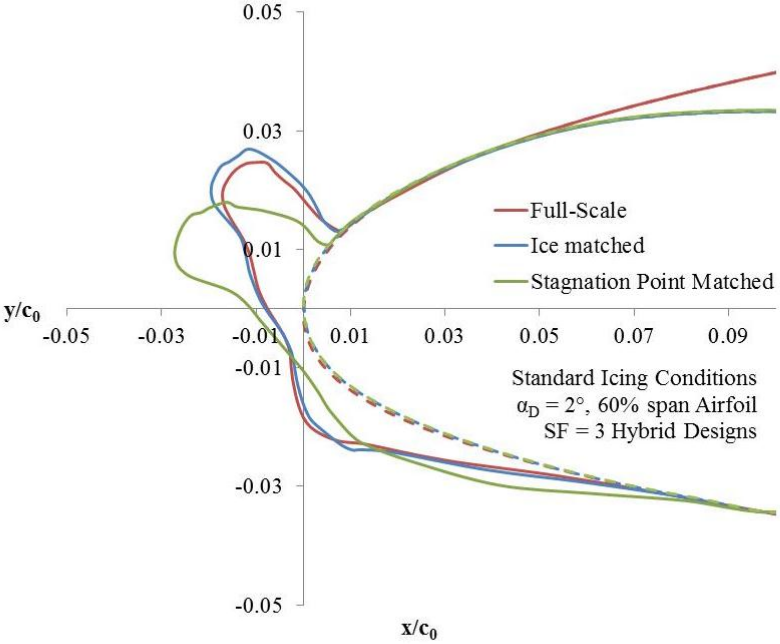

Fig. 3.23 Ice shape comparison between the standard hybrid and stagnation point matched designs.

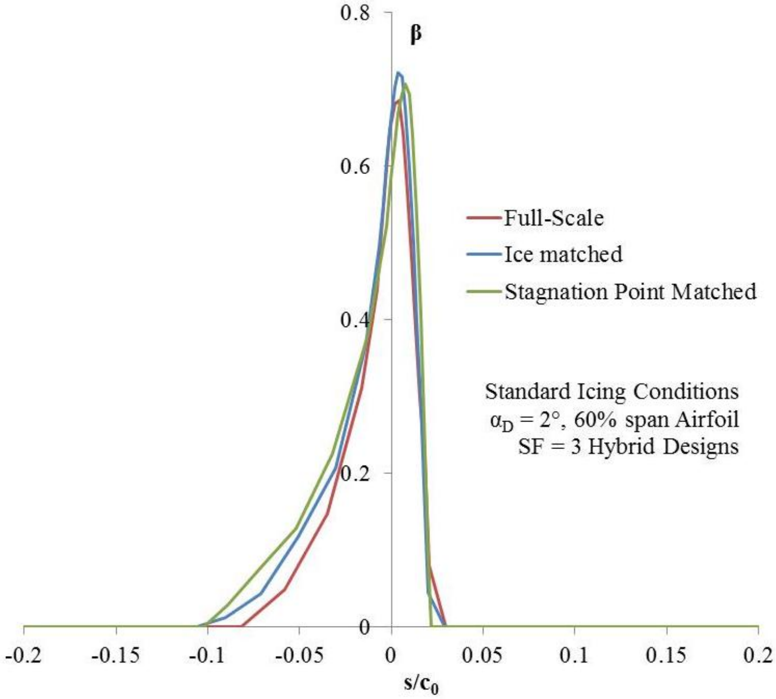

Fig. 3.24 Droplet impingement distributions for matched stagnation point and matched ice hybrid designs.

4. *Variation in Icing Conditions*

In addition to considering a range of angles of attack, most aircraft need to be tested over a range of icing conditions for safety in all mission phases. Changes in icing conditions, such as temperature, liquid water content, and median volume droplet diameter, can have an effect on the size and shape of the accreted ice. These changes can affect the ice accretion limits and growth, which may necessitate changes in the hybrid design. The most accurate method would be to create a hybrid design for each flight condition; however, that is almost never feasible based on model construction costs. Testing the hybrid design at the upper and lower bounds of the icing conditions will help ensure a well-designed model.

The temperature of the icing condition has an effect on the type of ice shape that is accreted on the surface. Colder temperatures tend to produce rime ice that conforms to the surface of the airfoil, while warmer conditions have a tendency to produce protrusions in the form of horn ice.[1] All of the ice accretion simulations done to this point have been run at a warmer temperature of 20° F (-7° C). This was to be certain of the formation of an ice horn, which was more easily matched between the full-scale and hybrid airfoil and is considered to be a more critical case. Figure 3.25 shows the 60% span CRM airfoil run at a lower temperature of -13° F (-25°C). The ice shape is well matched at this lower temperature with no adjustments made to the hybrid design.

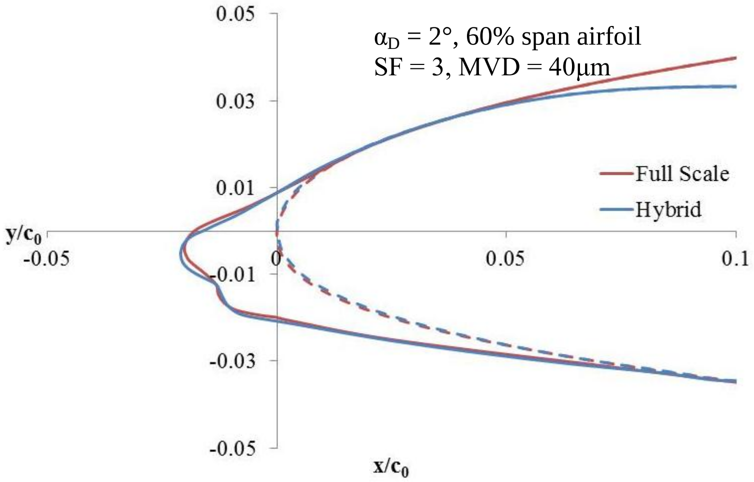

Fig. 3.25 Ice shape generated at -13° F for the 60% span CRM65 airfoil full scale and hybrid.

Changes to droplet size also affect the ice shape accreted on the airfoil surface and more importantly the ice accretion limits. Large 40μm droplets have been used for all previously presented simulated ice shapes in this work, but 15-20μm droplets are often tested as well. Large droplets produce the largest ice shapes for a given LWC, which make them easier to compare and require larger leading-edge extents, but small droplets are more susceptible to the changes in the flowfield and could require adjustments to the hybrid design. The simulated ice shape for 20μm droplets is shown in Fig. 3.26 for the full scale 60% span CRM and hybrid with scale factor 3. The accreted ice shape is much smaller than for the larger droplet conditions. An airfoil designed for these conditions would require much shorter leading edge extents and could accommodate a higher SF.

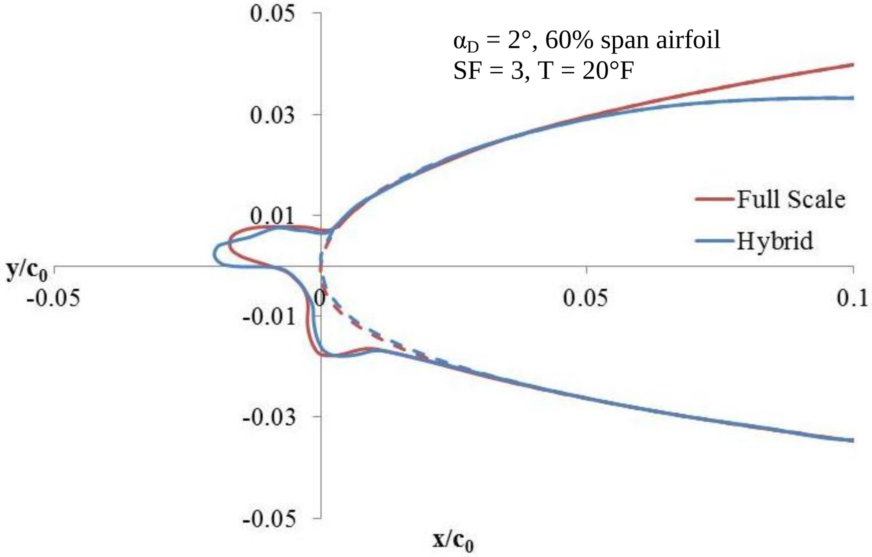

Fig. 3.26 Ice accretion for 20μm droplets on the full scale and hybrid 60% span CRM airfoil.

D. **Use of Flap in the Hybrid Design Method**

The addition of a flap to a hybrid airfoil design allows for the adjustment of the circulation of the airfoil without changing the angle of attack and in turn the leading-edge geometry. Once a hybrid design is set, a flap can be used so a single model can be used over a range of angles of attack. Adjustments in the flap deflection and angle of attack can be used together to add flexibility to the design. Early truncated airfoil designs added a simple flap to the full scale leading edge.[3] In the following studies, a simple flap is used; however, a more advanced flap can be designed and added to a hybrid design to improve the effectiveness of the flap if large changes in lift and circulation are required.

1. *Comparison of symmetric flapped and cambered hybrid design*

The symmetric flapped airfoil is a simplified design that was discussed with the alternative hybrid design in the research methods chapter. Figure 2.4 compared the standard cambered and symmetric flapped hybrid designs for the outboard wing section. A model built for a symmetric flapped design may be less complex and less expensive to design and build than one built for the more complicated cambered design. The symmetric flapped design relies on the flap effectiveness to achieve the correct airfoil circulation and may be more prone to separation at higher angles of attack due to adverse gradients already present on hybrid designs. In order to investigate the effectiveness of the flap on the hybrid design, cambered and symmetric flapped designs were created to match the LEWICE generated ice shapes of the full-scale airfoil. These studies were performed at 0, 2, 4, and 6° angle of attack.

The simple flapped models were designed from a hybrid airfoil with a symmetric aft section. For this analysis, a simple flap is added with the XFLR5 program,[18] with the hinge at 0.25 $x/c_{0.}$ The flap angle was set for each angle of attack by matching the lift coefficient of the cambered hybrid designed for the selected angle of attack. This matched lift design was then modified by adjusting the flap by one degree in each direction until the LEWICE generated ice shape provided a good match. The matched ice flap deflection, and matched lift flap deflection for each angle of attack is listed in Table 3.2. For each α_D, the cambered, angle of attack specific hybrid design and symmetric flapped hybrid design, with matched ice shape flap setting, are shown in Figure 3.27.

Table 3.2 Flap Deflection Angles of the Symmetric Flapped Hybrid Design

	Flap Deflection		Circulation ($\Gamma/u_\infty c_0$)	
α_D	matched ice	matched lift	matched ice	matched lift
0°	3°	8°	0.0117	0.0762
2°	7°	13°	0.1090	0.1652
4°	9°	20°	0.1580	0.2233
6°	17°	25°	0.2340	0.2670

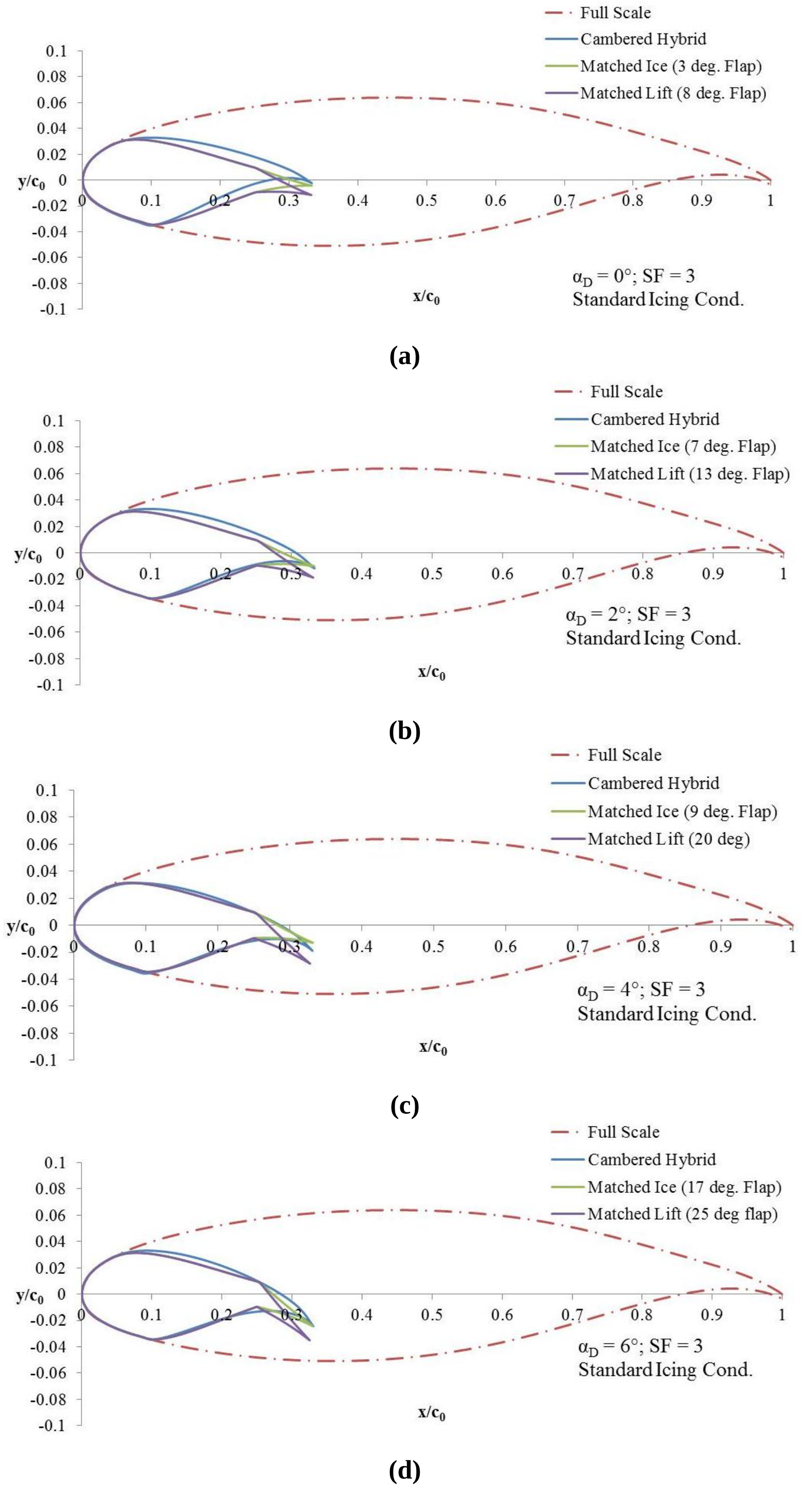

Fig. 3.27 Hybrid cambered and symmetric flapped designs for the CRM 60% span airfoil.

For all four angles of attack, the matched ice flap angle was lower than the matched lift flap angle. This difference is related to the dependence of circulation required on the design of the aft section of the airfoil. For most low to moderate angles of attack, the symmetric flapped design was able to model the full-scale ice shape with a certain flap angle. At 2° angle of attack, the ice shape was matched with a 7° flap deflection while lift was matched with a 13° flap deflection. Figure 3.28 shows LEWICE generated ice shapes for the full-scale ice shape, the cambered hybrid design, and the symmetric flapped designs for matched lift and matched LEWICE ice shapes. The 6° change in flap produced a significant change in ice shape where the upper horn for the matched lift case was too far forward due to the higher circulation.

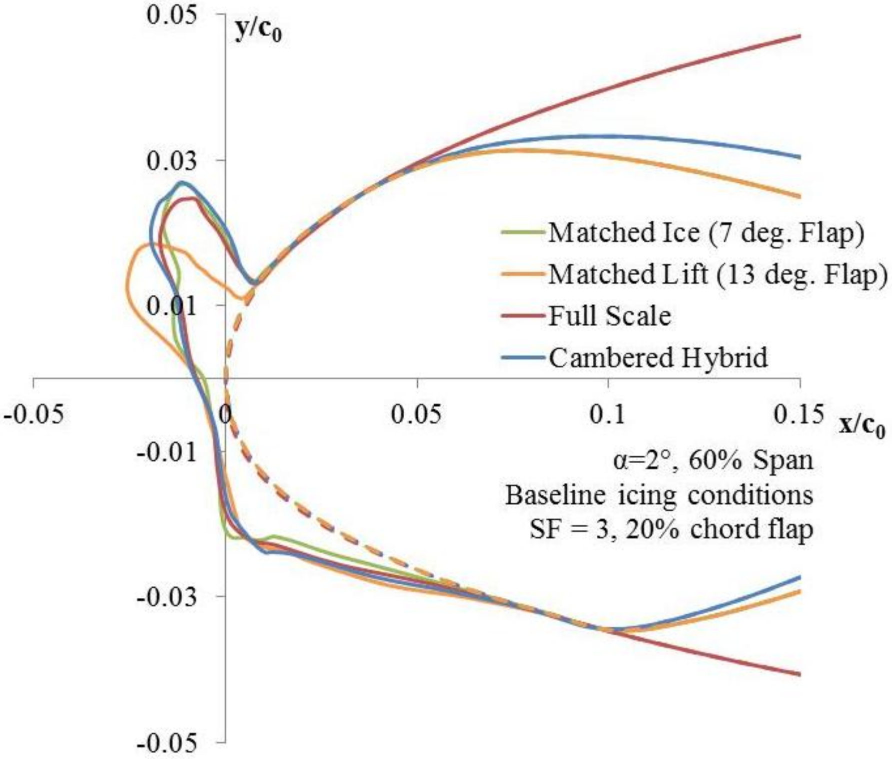

Fig. 3.28 Ice shapes comparing cambered and symmetric flapped hybrid designs at α_D=2°.

At α_D = 6°, the horn angle approaches 0°, and the change in ice shape due to flap deflection becomes smaller, so the accuracy of the ice shape was less sensitive to the flap angle, as seen in Fig. 3.29. A flap deflection of 17° was required to match the full scale ice shape, while the lift was matched at a flap deflection of 25°, however there is only a small change in ice shape over this 8° range. This was an inviscid analysis, and viscous effects would decrease the flap effectiveness with the possibility of separation or stall. At angles of attack higher than 6°, the hybrid design required much larger flap deflections to simulate the correct ice shapes. Advanced flaps may be needed to model ice accretion at higher angles of attack. Figure 3.29 shows the ice shapes generated for the full-scale and hybrid airfoil designs.

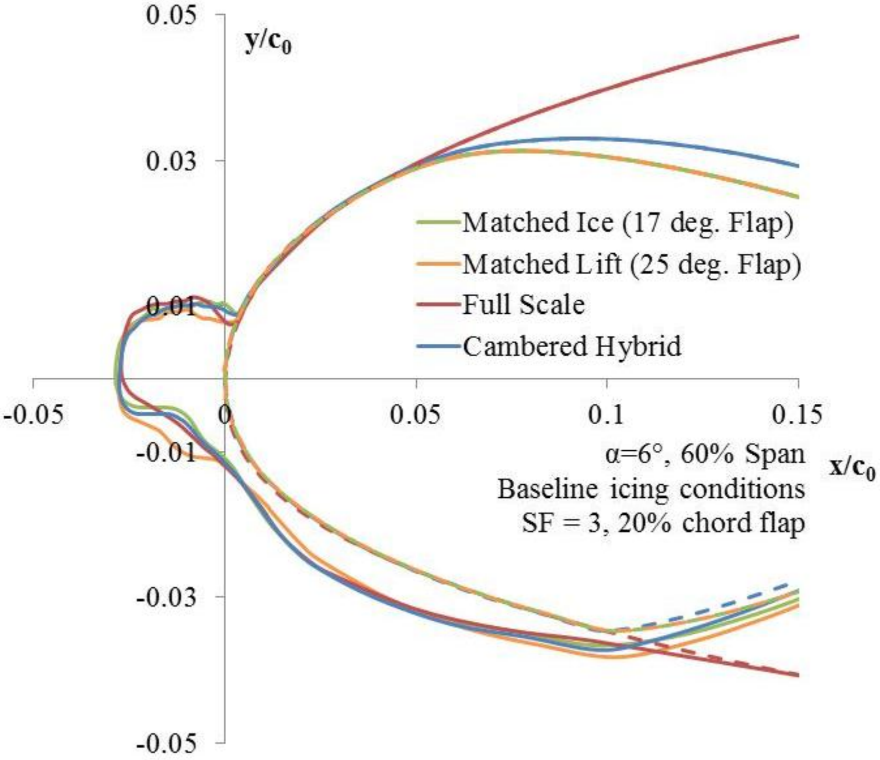

Fig. 3.29 Comparisons of ice shapes for hybrid designs at $\alpha_D = 6°$.

2. *Use of flap for off-design conditions*

As a compromise between the simple symmetric hybrid design and the cambered design at each angle of attack, a flap can be added to a cambered hybrid airfoil to match icing conditions at off-design cases. The same flap design considerations apply as with the symmetric flapped design, but the deflection angles are much smaller. The flap added to the cambered designs studied here matched the aft section of the cambered airfoil and is hinged at 0.25 x/c_0, like the symmetric flapped design. At angles of attack lower than $\alpha_{D,}$ the flap should be deflected trailing-edge up, and at higher angles of attack, a downward deflection is necessary. Starting from the cambered hybrid design with $\alpha_D = 2°$, a flap can be deflected to improve the ice shape over a range of angles of attack. For lower angles of attack, such as the 0° case shown in Figure 3.30, the flap angle is set negative, to reduce the circulation. This lowers the suction peak and tilts the ice horn higher on the airfoil surface. For higher angles of attack, like the 6° case shown in Figure 3.31, the flap is set trailing edge down to increase the circulation. Both of the flapped designs match the full-scale on-design case well, with flap deflections which are less than the deflections for the symmetric design. The 0° case requires a flap deflection of 4° up (δ_f = -4°), and the 6° case requires an 8° flap deflection downward (δ_f = 8°).

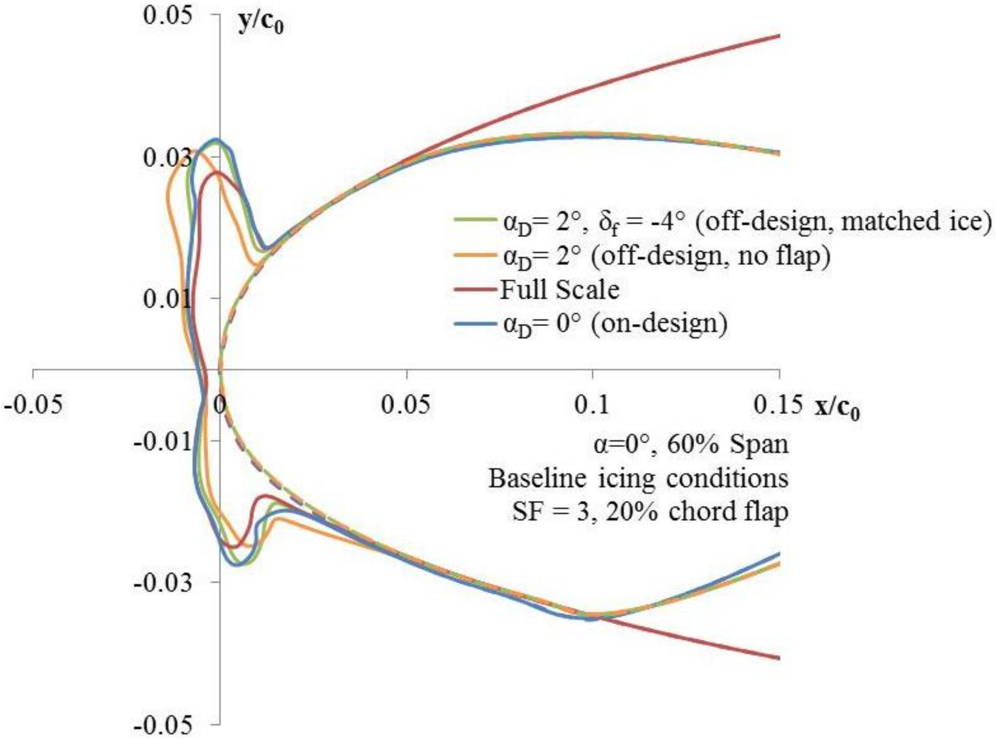

Fig. 3.30 **α = 0° ice shapes for full scale, α_D=0° cambered design, and α_D=2° cambered and flapped designs.**

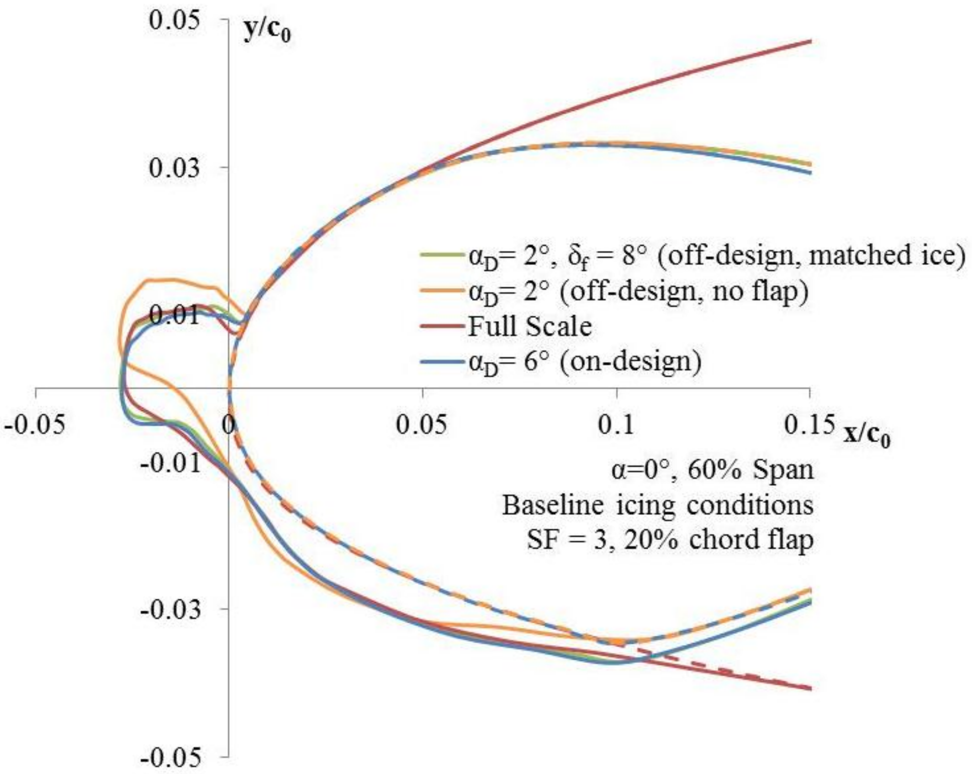

Fig. 3.31 $\alpha = 6°$ ice shapes for full scale, α_D=6° cambered design, and α_D=2° cambered and flapped designs.

Ice shapes can also be matched at off design conditions through adjusting the hybrid airfoil angle of attack instead of adding a flap. To correctly match the ice shape, the circulation must be increased or decreased as with the flapped corrections. In order to match the full scale accretion at $\alpha = 4°$, the hybrid airfoil with $\alpha_D = 2°$ is set at $\alpha_{nose} = 4.5°$. The resulting ice shapes for the full scale accretion as well as the hybrid at adjusted angle of attack are shown in Fig. 3.32. This adjustment also produces a fairly accurate result; however, the droplets are not encountering the correct full scale geometry, so this technique may not work as well for larger droplets or higher velocities where leading edge geometry becomes more important.

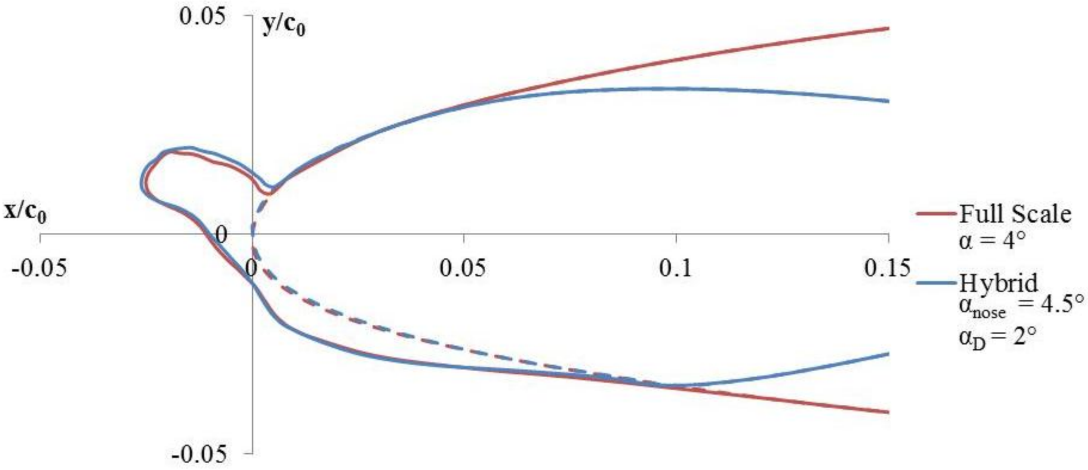

Fig. 3.32 **Full scale and hybrid ice accretions for α = 4°, with off design hybrid corrected with angle of attack adjustment.**

E. Effects of Tunnel Walls on Airfoil Ice Accretion

The effect of wind tunnel walls on aerodynamic tests of airfoils and wings is well documented, and can be estimated using aerodynamic performance variables.[23] However, calculating the effect on droplet trajectories and impingement on airfoils is not as well known. For the full-scale airfoils used in this study, the tunnel blockage was much higher than the acceptable limits of normal aerodynamic tests. Since the CRM65 and IRT are representative of common wings and tunnels used in this research, most large swept wings will have similar blockage problems.

1. *Aerodynamic corrections and wind tunnel blockage*

Wind tunnel wall corrections provide a first order estimate of the wall effects on the flowfield and droplet trajectories. The wind tunnel blockage corrections for airfoil testing were calculated using methods from Barlow, Rae, and Pope.[23] Solid blockage, which characterizes the increase of velocity around the model as the model is confined by the wind tunnel walls, was calculated for mostly two-dimensional models using the following equation. In this equation, K_1 is a constant, equal to 0.52 for models installed vertically in a tunnel, V is the model volume, and A is the tunnel test section area.

$$\varepsilon^{sb} = \frac{K_1 * V}{A^{3/2}} \qquad (4)$$

Solid blockage is only part of the blockage, and remains constant regardless of flow and angle of attack. Wake blockage, ε^{wb}, measures the increase in velocity around the wake to maintain a mass flow rate while the fluid in the wake slows down. The wake blockage was calculated from an uncorrected drag coefficient, C_{du}, and the ratio of tunnel height to model chord, h/c. The wake blockage was given by:

$$\varepsilon^{wb} = \frac{C_{du}}{2^{h}/_{c}} \qquad (5)$$

The total blockage, ε_t, is the sum of solid blockage and wake blockage and was used to estimate the corrections for velocity, lift, and drag of the model. Table 3.3 catalogs the values of h/c, solid blockage, wake blockage, and total blockage for hybrid designs at the various span stations, discussed in the section on variation in chord, and a range of SF.

Table 3.3 Wind tunnel blockage for CRM airfoils and hybrid design

Airfoil	Hybrid Scale	h/c	ε_{sb}	ε_{wb}	ε_{total}
22% span	1	0.45	0.2215	0.0055	0.2270
60% span	1	0.9	0.0596	0.0033	0.0629
90% span	1	1.5	0.0209	0.0023	0.0232
60% span	2	1.8	0.0167	0.0011	0.0178
60% span	3	2.7	0.0104	0.0005	0.0109
60% span	4	3.6	0.0064	0.0003	0.0067
60% span	5	4.5	0.0047	0.0003	0.0050

When considering the effects of tunnel walls on the ice shapes, there were two additional parameters of interest based on aerodynamic wall correction methods. The first was the corrected tunnel velocity, which affected the droplet inertia parameter, and the second was the airfoil circulation, which was directly related to the lift coefficient. The lift coefficient changed due to the increased velocity over the upper surface of the airfoil, but it also changed due to streamline curvature caused by the constraints of the walls. Effects of streamline curvature are discussed in detail in Barlow, Rae, and Pope, but the simple angle of attack correction, and then lift coefficient correction are given here, where σ is the simplified parameter, $\frac{\pi^2}{48}(^{h}/_{c})^{-2}$:

$$\Delta\alpha_{sc} = \frac{\sigma c_l}{2\pi} \qquad (6)$$

$$\Delta C_{l,sc} = \sigma C_l \qquad (7)$$

Combining these corrections with the blockage corrections, the corrections for velocity, V, and lift coefficient, C_l, are:

$$\frac{V}{V_u} = (1 + \varepsilon_t) \qquad (8)$$

$$\frac{C_l}{C_{l,u}} = (1 - \sigma - 2\varepsilon_t) \qquad (9)$$

Table 3.4 lists the estimated change in velocity and lift coefficient for each of the airfoils listed in Table 3.3.

Table 3.4 Estimate of Change in Velocity and Lift Coefficient Due to Wall Effects

Airfoil	SF	ΔV	ΔC_l
22% span	1	22.70%	143.40%
60% span	1	6.29%	37.97%
90% span	1	2.32%	13.78%
60% span	2	1.78%	9.91%
60% span	3	1.09%	5.00%
60% span	4	0.67%	2.93%
60% span	5	0.50%	2.01%

2. *Tunnel Effects on C_P*

In the previous section, wall correction theories were applied to model blockage values likely to be seen in icing testing. For the remainder of this chapter, the wall effects will be directly calculated using the TUNDROP droplet impingement program.[20] Wind tunnel walls changed the C_P distribution over the surface of the airfoil. This changed the airfoil circulation, which can change the overall flowfield and the impingement, as well as the velocity on the airfoil surface, which can change the way the ice accretes. Due to wall effects, the velocity on the upper surface generally increased, which raised the suction peak on the upper surface. The example hybrid airfoil, 60% span CRM65 with scale factor of 3, was placed between the wind tunnel walls of the Icing Research Tunnel, set ten feet apart, which gives an h/c of 3. Figure 3.33 shows C_P plots for the hybrid airfoil with tunnel walls and in free air, along with the full-scale airfoil in free air for reference.

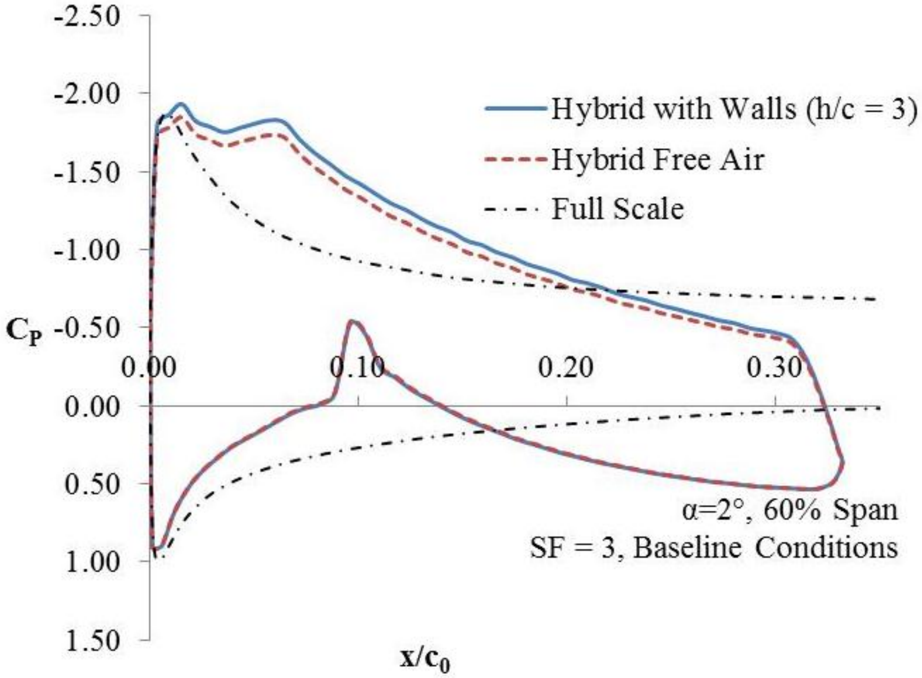

Fig. 3.33 C_P plots for the CRM 60% span hybrid with tunnel wall effects.

The decrease in C_P for the wall model was consistent with the wind tunnel wall corrections calculated in the previous section. This decrease of pressure on the upper surface is directly proportional to the tunnel height. As the walls were set farther away from the CRM hybrid, for example at an h/c of 6, the walls had little effect. As the tunnel walls were brought closer to the model at an h/c less than 1, the minimum C_P decreases by over 50%. As the tunnel wall effects grew, shown in Fig. 3.34, the pressure peak at the upper surface junction between the full scale and hybrid scale became more important, and the adverse pressure gradient on the back half of the airfoil became more severe, increasing the possibility of separation.

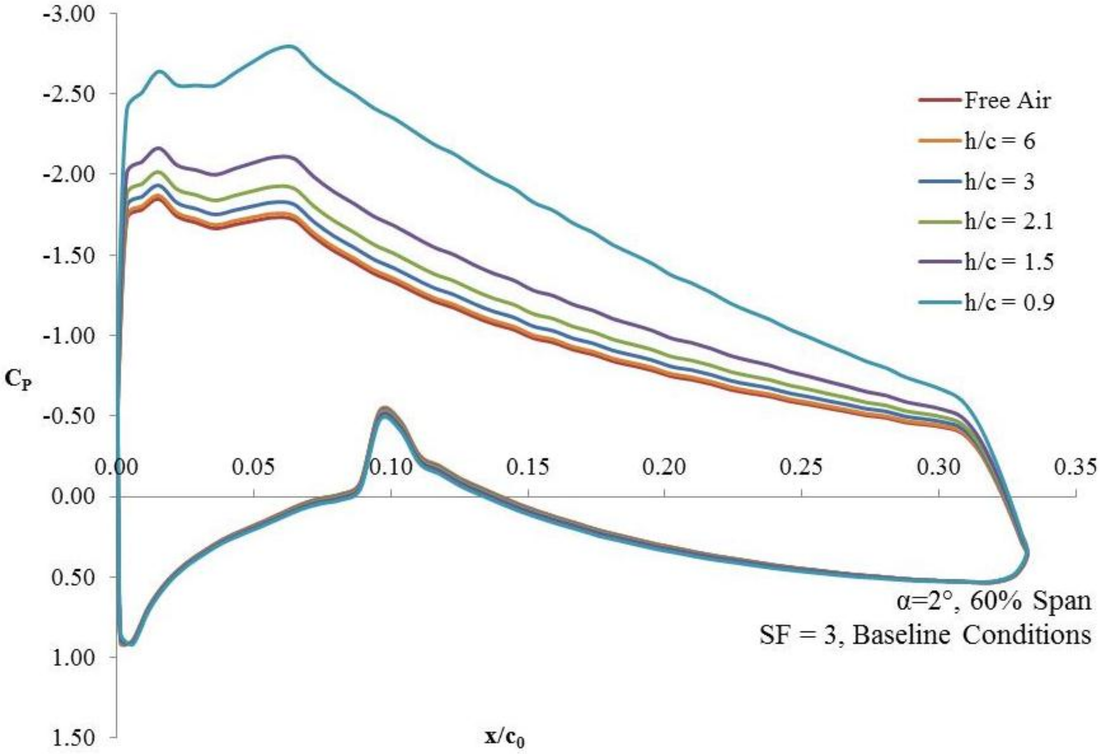

Fig. 3.34 Changes in C_P distribution for increasing wall effects.

Comparing the wall effect on the hybrid model to the effect on the equivalent full-scale model provided some evaluation of the advantage of the hybrid model. C_P distributions of the full scale 60% span CRM and the hybrid design with scale factor of 3 are compared in Fig 3.35. The full-scale minimum C_p decreased by 18% with the wall effects, while the hybrid design C_P between the same walls decreased by 5%.

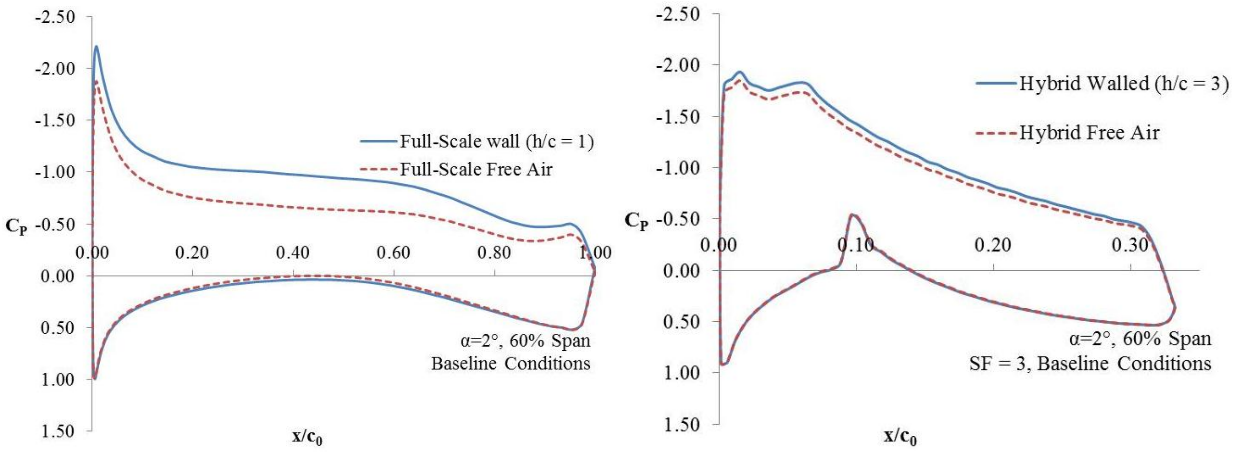

(a) **(b)**

Fig. 3.35 Tunnel wall effects on the C_P for the (a) full scale 60% span and (b) hybrid airfoils.

The C_P distributions generated by TUNDROP for hybrid airfoils with α_D = 0, 2, 4, and 6°are shown for the case between walls with h/c = 3 in Figure 3.36. As the angle of attack increased, the wake blockage and wall effects increased slightly. However, for tunnel walls with h/c = 3, the change in minimum C_P was never more than 5%. The wall effects did not significantly increase the adverse pressure gradient on the upper surface or at the leading edge and aft section junction on the lower surface. The free-air solution is shown for each case with a matching dashed line. The change due to wall effects is much smaller than the change due to angle of attack for each case.

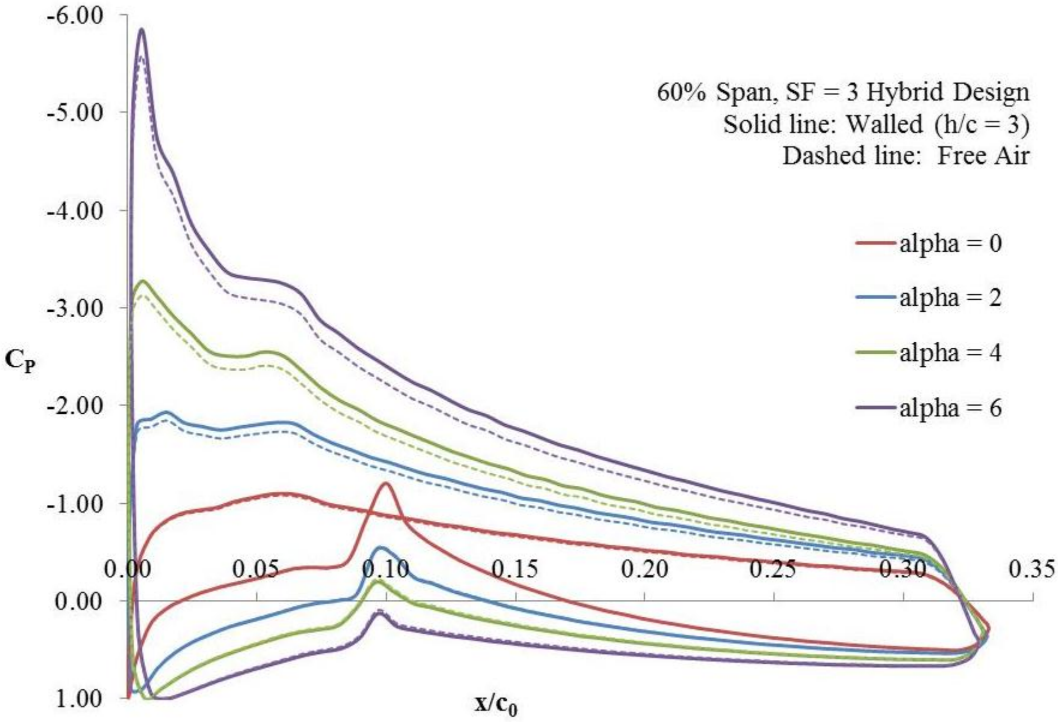

Fig. 3.36 Tunnel wall effects for CRM hybrid airfoils at angles of attack from 0° to 6°.

3. *Tunnel Effects on Droplet Impingement*

The droplet impingement on the hybrid airfoil is the closest estimate to the actual ice shape that can be determined for two-dimensional wall effects using the TUNDROP code. As of now, there is not a convenient method to include wall effects in a LEWICE2D analysis. Previously, it was shown that if the β distributions and leading-edge flowfield are matched, the base ice shape will match. For cases with lower blockage, as described in the previous section, the changes in velocity are low enough that matching the β curve should predict the correct ice shape. The free air and in tunnel β curves are shown for the CRM hybrid airfoil in Figure 3.37 with the full-scale airfoil free-air curve. There was an increase in the maximum collection efficiency, and a small shift in β toward the upper surface. Based on earlier calculations using LEWICE2D, the ice horn was predicted to be larger as β_{max} increased and may have a small error in the horn angle. The change in the collection efficiency curve due to the wall effect is similar to the change between the full-scale and hybrid design seen in the previous sections. The error due to wall effects is shown to be of the same order of magnitude as the error due to the hybrid design.

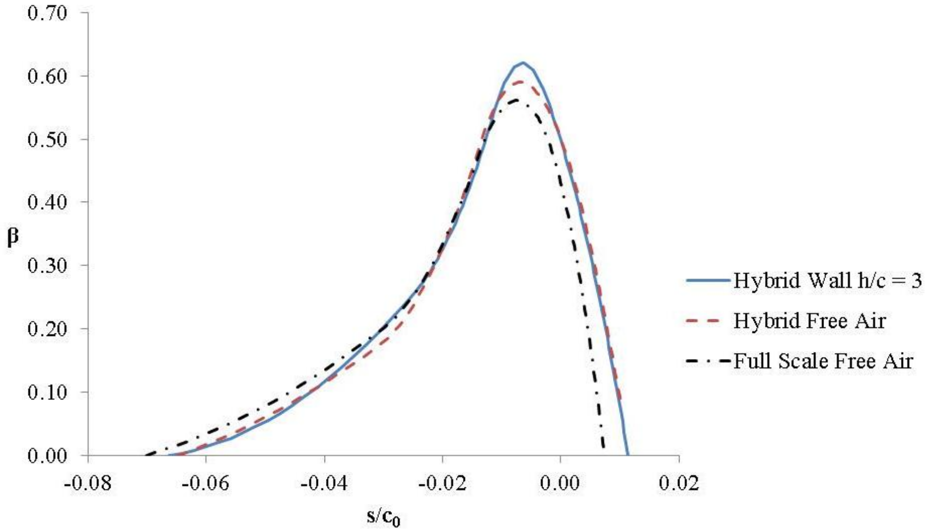

Fig. 3.37 Collection efficiency for CRM 60% span airfoil and scale factor 3 hybrid.

As the wall distance decreased from an h/c = 6 to an h/c = 2, the maximum β increased, but the location of the maximum remains fairly constant. This would lead to larger ice horns as the walls narrow. However, for walls with an h/c less than 2, the behavior became much less predictable, as shown in Fig. 3.38. The maximum β decreased and for h/c = 1.5, but then increased again for h/c = 0.9. The β curve for h/c = 0.9 was also shifted slight toward the lower surface, indicating a slightly larger error in the horn angle from the tunnel effects. Figure 3.38 shows the collection efficiencies for all of these cases. Models with a larger h/c and smaller h/c are plotted separately. The increasing trends for low h/c are consistent with the data presented by Bragg and Wells.[22] For a significant increase in lift and change in C_P, there was only a small increase in β and almost no qualitative change to the shape of the β distribution. This lack of change was attributed to the streamline curvature and the constriction of farfield droplet trajectories by the tunnel walls. For higher blockage tests, such as h/c = 0.9 and h/c = 1.5 cases shown in Fig. 3.34, the effect of the change in velocity field may be more important than the change due to trajectory curvature. These higher blockage cases need more study, with more advanced tools.

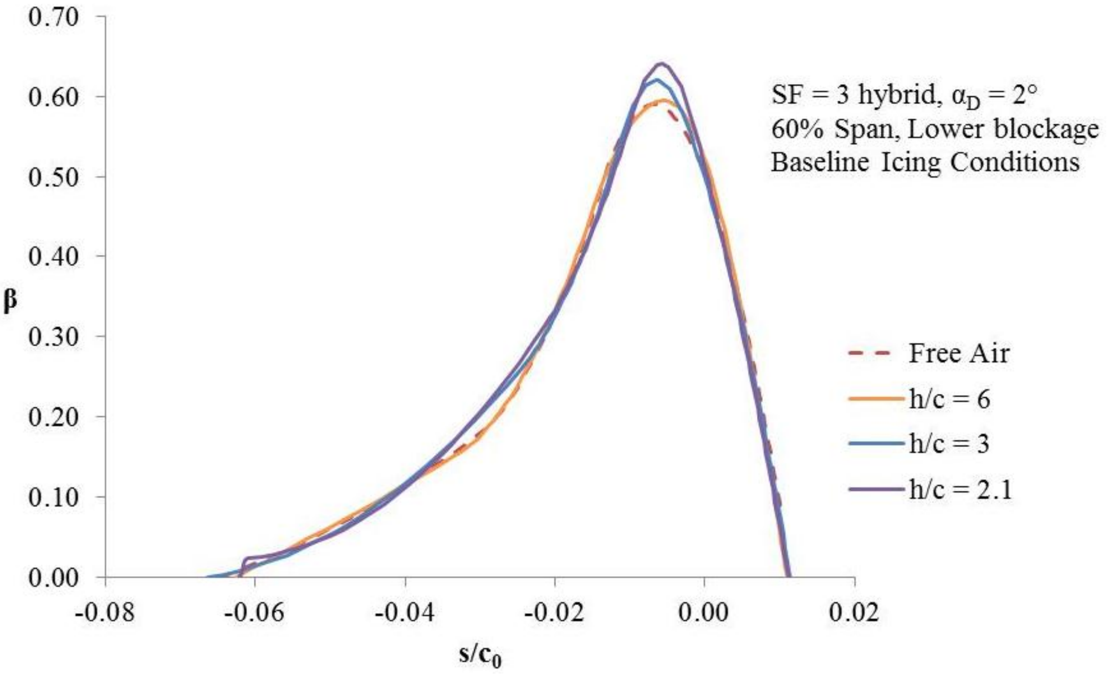

(a)

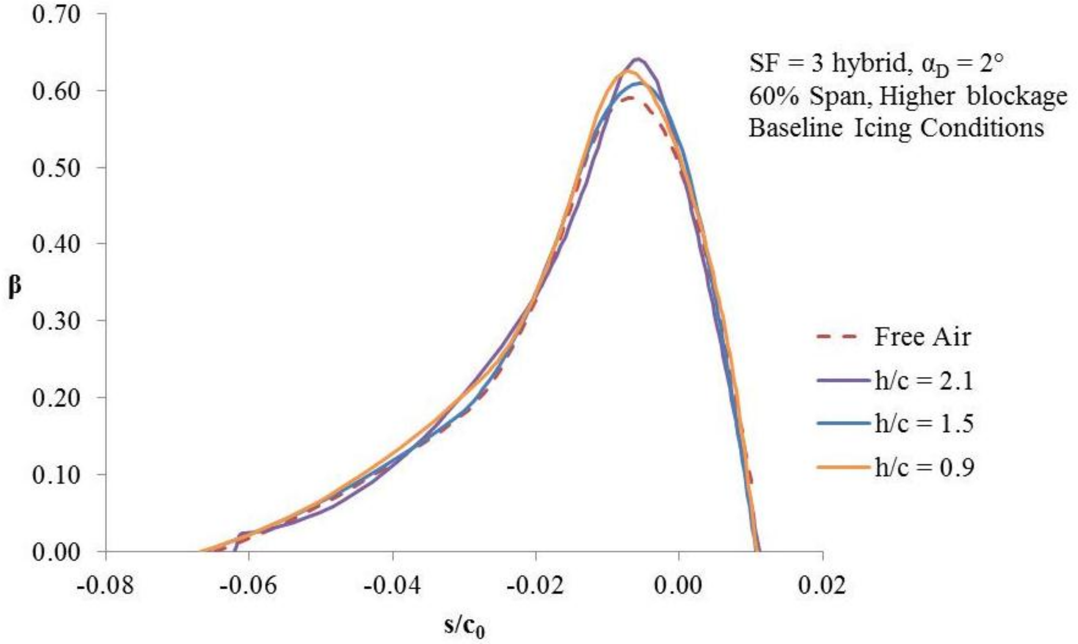

(b)

Fig. 3.38 Collection efficiency for the CRM hybrid airfoil at relatively (a) low and (b) high tunnel blockage.

4. *Design in the Presence of Walls*

To reduce the error due to the tunnel wall effects, modifications can be made to the hybrid design method by adjusting the circulation and suction peak of the hybrid airfoil. Because the suction peak increased with the inclusion of tunnel walls, deflecting a flap to reduce the peak by the same percentage may offset some of the wall effect. Deflecting the flap up 1° on the cambered hybrid airfoil for the $\alpha_D = 2°$, h/c = 3 case reduced the suction peak in the tunnel to match the free-air, unflapped airfoil. Figure 3.39 compares the flapped 'corrected' airfoil in tunnel C_P distribution to the in tunnel and free air C_P distribution for the standard cambered hybrid design. The β distribution for the flapped airfoil, shown in Fig. 3.40, does not match the free air β distribution as well. This was because the change in flap angle accounted for the change in upper surface velocity and circulation without correcting for streamline curvature. While the wall effects on C_P could be accounted for, adjusting for the differences in droplet impingement was more difficult. Fortunately, the wall effects on impingement were much smaller due to offsetting errors.[22] For most design cases, with h/c larger than 2, based on inviscid estimates, no design modifications should be necessary for testing in a tunnel. There may be small errors due to the wind tunnel walls, which will increase β_{max} and circulation, but these errors are comparable to the design error and error in LEWICE simulation. However, for fully three dimensional models, three dimensional and viscous effects may result in tunnel effects not modeled here. CFD analysis and comparisons with LEWICE 3D can help to determine if tunnel corrections will be needed for the actual three dimensional design.

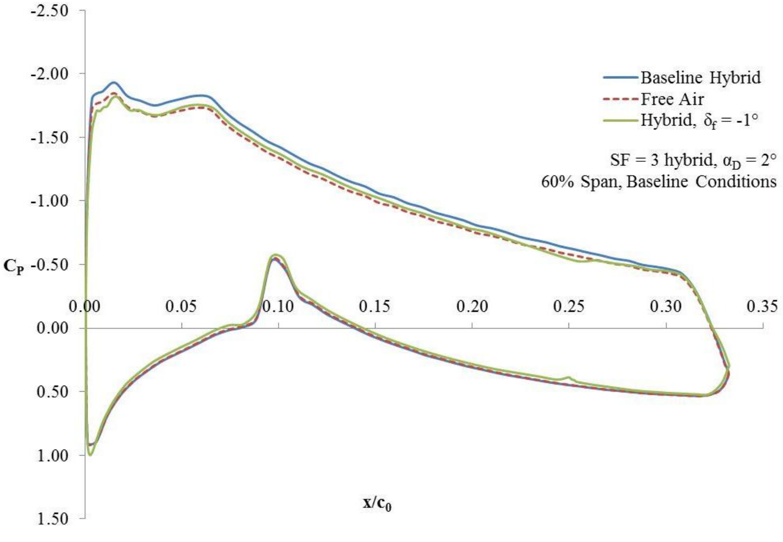

Fig. 3.39 Tunnel effects on hybrid C_P distribution with corrected flapped hybrid design.

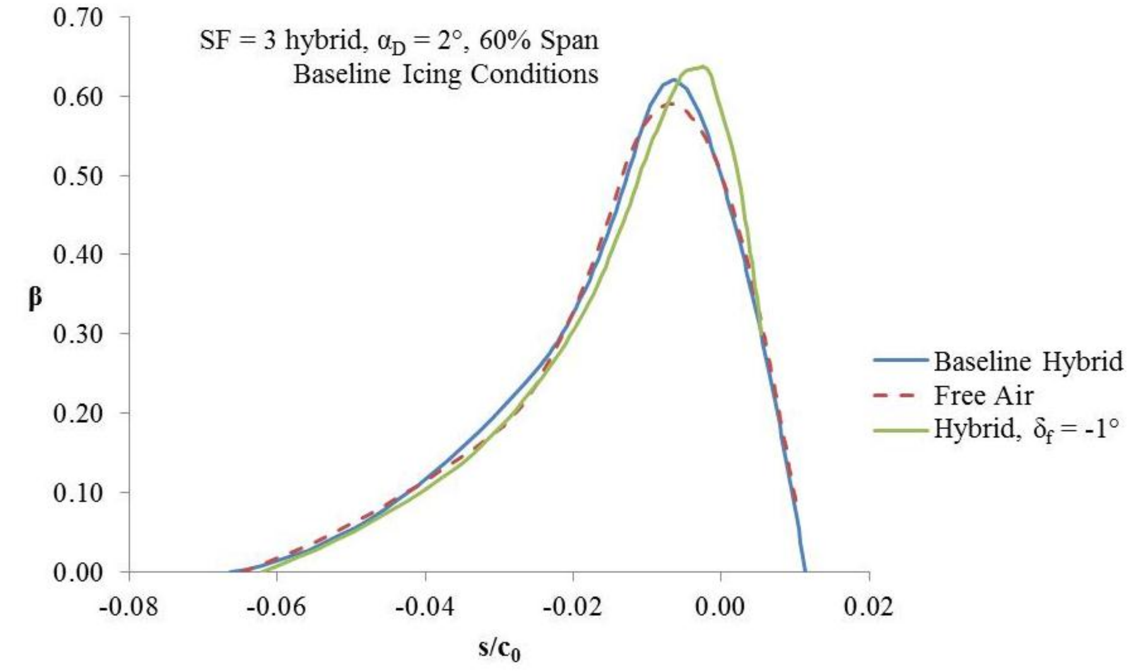

Fig. 3.40 β distribution for the hybrid design in tunnel and flapped 'corrected' design.

IV. Summary, Conclusions, and Recommendations

A. **Summary**

The two-dimensional hybrid design method was explored for use in acquiring full-scale ice accretions on large swept wings in a standard icing tunnel. The selected airfoils were taken from cuts normal to the leading edge of the airfoil for the Common Research Model three-dimensional swept wing. Three cuts were selected at 22%, 60% and 90% span, and then tested with XFOIL and LEWICE2D. The predicted ice shapes and impingements were compared to determine the accuracy of the hybrid designs. Designs were made and tested over a range of angles of attack and icing conditions.

The circulation and C_P distributions were also compared to determine the effect of these variables on the predicted ice shape. A symmetric design was also created to match the predicted ice shape by deflecting a flap for a range of angles of attack. A flap was added to a cambered hybrid design to match the ice shape at other angles of attack. Finally, the TUNDROP code was used to calculate the inviscid tunnel effects on the hybrid airfoil C_P and droplet impingement distributions.

B. **Conclusions**

1. A well-designed hybrid airfoil with matched leading edge C_P and droplet impingement distribution will provide a matched LEWICE predicted ice shape.
2. Adjusting the nose droop and C_{m0} both change the airfoil circulation and can be used to create an effective design. Nose droop increased circulation by moving the trailing edge, while C_{m0} changed circulation by adding camber while keeping the leading edge and trailing-edge constant.
3. Moderate values of C_{m0} and nose droop will prevent severe adverse pressure gradients aft of the leading-edge extents.
4. Larger airfoil sections can be designed with a higher SF and shorter leading-edge extents while shorter airfoil sections require longer leading-edge extents but a lower SF. The larger airfoil section has a smaller nondimensional ice accretion, which requires shorter leading-edge extents. This airfoil has a higher blockage, so with the shorter leading-edge extents, the SF can be increased. The shorter chord leads to larger nondimensional ice accretions, which require larger leading-edge extents and a lower SF.

5. As α_D increases, the nose droop and C_{m0} must also be increased to match the predicted ice shape. The full-scale airfoil circulation increases, so the circulation of the smaller hybrid design must also be increased to account for the change in predicted ice shape.
6. As the SF increases, the required nondimensional circulation decreases, and the stagnation point moves forward. The upper surface C_P is the best indication of ice shape matching.
7. Circulation is not unique to the accuracy of the ice shape, because multiple designs can match the predicted ice shape, but have different circulations.
8. A symmetric design with a simple flap will match ice shapes over a range of angles of attack, but is potentially limited by viscous effects on the flap effectiveness due to the large flap deflections needed at high angles of attack.
9. A simple flap added to a cambered design allows for ice shape matching at off-design angles of attack.
10. Adding tunnel walls increased the airfoil circulation as the walls neared the body, but did not change the C_P by more than 10% for h/c greater than 2.
11. For h/c greater than 2, the droplet impingement is not greatly affected by the presence of the walls due to offsetting circulation and streamline curvature effects.
12. The addition of a flap to attempt to correct for tunnel wall C_P effects led to increased error in the droplet impingement.

C. **Recommendations**

1. Advanced flap design for the hybrid airfoil should improve the off-design performance of the hybrid design, allowing hybrid designs at higher angles of attack. The hybrid flap has much more design freedom than a standard flap system, because the flap will not have to fit into a cruise airfoil geometry.
2. Further studies should be made into flap design for hybrid airfoils, including the possible use of vortex generators or suction to prevent flow separation.
3. Further investigation into the relationship between the hybrid flow-field and ice accretion would lead to better testing techniques for hybrid airfoils.

4. A three-dimensional analysis of the flowfield and ice accretion should be done to validate the two-dimensional methods and test the validity of the assumption of locally two-dimensional flow in the hybrid design.
5. A calculated flow-field that can be input into the LEWICE program would aid in determining the effect of the change in circulation due to tunnel walls on the accretion of the predicted ice shape.
6. Developing an optimization strategy by automating XFOIL, AIRDROP, TUNDROP, and LEWICE into the same design run should be developed to potentially improve the process and provide more accurate designs. Running multiple designs over a range of conditions may begin to show more of a pattern that would give more clues to the relationship between the icing conditions, flow field, and ice accretion.
7. Using in-tunnel CFD calculations and LEWICE 3D, further investigation should be conducted to find three-dimensional and viscous tunnel wall effects and possible corrections necessary for accurate droplet impingement and ice accretion.

Appendix A List of Airfoil Coordinates for CRM Sections

Table A.1 22% Span Perpendicular Airfoil Coordinates (Chord = 235.8 in)

22% Span Airfoil					
x	**y**	**x**	**y**	**x**	**y**
1.00000	0.00071	0.21509	0.05765	0.28208	-0.05066
0.99092	0.00295	0.19203	0.05555	0.30537	-0.05126
0.97327	0.00668	0.16904	0.05302	0.32872	-0.05149
0.95177	0.01049	0.14620	0.05007	0.35215	-0.05138
0.92904	0.01409	0.12357	0.04667	0.37561	-0.05093
0.90579	0.01742	0.10128	0.04279	0.39914	-0.05018
0.88229	0.02049	0.07960	0.03839	0.42271	-0.04913
0.85864	0.02336	0.05903	0.03347	0.44634	-0.04781
0.83482	0.02607	0.04083	0.02823	0.47003	-0.04625
0.81081	0.02868	0.02673	0.02323	0.49377	-0.04446
0.78665	0.03124	0.01706	0.01891	0.51756	-0.04246
0.76240	0.03378	0.01060	0.01520	0.54140	-0.04029
0.73815	0.03631	0.00622	0.01190	0.56528	-0.03795
0.71391	0.03883	0.00322	0.00883	0.58921	-0.03548
0.68973	0.04132	0.00130	0.00591	0.61319	-0.03288
0.66561	0.04376	0.00024	0.00311	0.63724	-0.03019
0.64155	0.04611	-0.00004	0.00046	0.66136	-0.02743
0.61757	0.04837	0.00057	-0.00210	0.68550	-0.02463
0.59362	0.05049	0.00216	-0.00465	0.70967	-0.02181
0.56970	0.05248	0.00489	-0.00705	0.73388	-0.01901
0.54580	0.05432	0.00879	-0.00939	0.75811	-0.01622
0.52190	0.05600	0.01436	-0.01189	0.78235	-0.01344
0.49802	0.05752	0.02269	-0.01479	0.80644	-0.01071
0.47414	0.05885	0.03560	-0.01843	0.83027	-0.00811
0.45028	0.06002	0.05386	-0.02279	0.85385	-0.00572
0.42647	0.06099	0.07525	-0.02728	0.87726	-0.00364
0.40272	0.06175	0.09769	-0.03146	0.90039	-0.00200
0.37901	0.06228	0.12050	-0.03526	0.92276	-0.00089
0.35538	0.06255	0.14345	-0.03867	0.94489	-0.00030
0.33179	0.06254	0.16648	-0.04170	0.96861	-0.00020
0.30828	0.06224	0.18952	-0.04431	0.99000	-0.00052
0.28486	0.06163	0.21258	-0.04652	0.99995	-0.00070
0.26151	0.06067	0.23570	-0.04831		
0.23827	0.05935	0.25886	-0.04969		

Table A.2 60% Span Perpendicular Airfoil Coordinates (Chord = 121.6 in)

60% Span Airfoil					
x	y	x	y	x	y
1.00000	0.00000	0.09581	0.03915	0.47572	-0.04770
0.99088	0.00322	0.07386	0.03504	0.50022	-0.04617
0.97407	0.00809	0.05411	0.03061	0.52467	-0.04434
0.95398	0.01278	0.03807	0.02618	0.54910	-0.04218
0.93178	0.01710	0.02622	0.02209	0.57353	-0.03972
0.90817	0.02109	0.01783	0.01841	0.59797	-0.03696
0.88362	0.02493	0.01183	0.01507	0.62245	-0.03391
0.85856	0.02876	0.00745	0.01192	0.64703	-0.03059
0.83339	0.03257	0.00427	0.00886	0.67172	-0.02703
0.80831	0.03634	0.00205	0.00585	0.69658	-0.02328
0.78340	0.04000	0.00067	0.00291	0.72155	-0.01940
0.75864	0.04348	0.00003	0.00007	0.74657	-0.01547
0.73404	0.04674	0.00011	-0.00264	0.77151	-0.01161
0.70953	0.04974	0.00098	-0.00534	0.79624	-0.00791
0.68507	0.05244	0.00272	-0.00809	0.82066	-0.00449
0.66065	0.05485	0.00545	-0.01078	0.84468	-0.00145
0.63621	0.05695	0.00926	-0.01335	0.86821	0.00106
0.61175	0.05873	0.01430	-0.01597	0.89124	0.00293
0.58721	0.06022	0.02123	-0.01874	0.91364	0.00400
0.56259	0.06143	0.03100	-0.02179	0.93524	0.00415
0.53788	0.06237	0.04489	-0.02521	0.95592	0.00327
0.51309	0.06306	0.06334	-0.02891	0.97499	0.00138
0.48825	0.06352	0.08506	-0.03251	0.99131	-0.00145
0.46336	0.06377	0.10827	-0.03579		
0.43847	0.06381	0.13210	-0.03870		
0.41360	0.06364	0.15625	-0.04124		
0.38871	0.06325	0.18061	-0.04346		
0.36386	0.06265	0.20511	-0.04539		
0.33907	0.06183	0.22963	-0.04702		
0.31434	0.06075	0.25423	-0.04836		
0.28962	0.05943	0.27884	-0.04942		
0.26490	0.05787	0.30345	-0.05019		
0.24023	0.05606	0.32810	-0.05069		
0.21564	0.05400	0.35275	-0.05090		
0.19112	0.05167	0.37739	-0.05084		
0.16677	0.04906	0.40200	-0.05049		
0.14267	0.04613	0.42660	-0.04985		
0.11893	0.04285	0.45118	-0.04892		

Table A.3 90% Span Perpendicular Airfoil Coordinates (Chord = 72.8 in)

90% Span Airfoil					
x	**y**	**x**	**y**	**x**	**y**
1.00000	0.00185	0.02279	0.01840	0.36346	-0.04656
0.98948	0.00593	0.01464	0.01481	0.40638	-0.04550
0.97887	0.00921	0.01096	0.01285	0.45490	-0.04327
0.96831	0.01207	0.00923	0.01181	0.50941	-0.03949
0.95782	0.01464	0.00759	0.01072	0.56624	-0.03415
0.93717	0.01910	0.00602	0.00956	0.62002	-0.02790
0.91695	0.02295	0.00455	0.00831	0.66934	-0.02134
0.89723	0.02638	0.00208	0.00559	0.71486	-0.01489
0.87799	0.02952	0.00114	0.00412	0.75698	-0.00889
0.84072	0.03529	0.00076	0.00334	0.79599	-0.00366
0.80488	0.04054	0.00045	0.00254	0.83217	0.00059
0.77046	0.04524	0.00021	0.00171	0.86567	0.00371
0.73732	0.04937	0.00006	0.00086	0.89666	0.00557
0.70545	0.05291	0.00000	0.00000	0.92524	0.00607
0.64538	0.05832	0.00003	-0.00086	0.95159	0.00511
0.58992	0.06183	0.00092	-0.00401	0.96406	0.00405
0.53868	0.06388	0.00280	-0.00684	0.97596	0.00260
0.49140	0.06484	0.00542	-0.00937	0.98722	0.00069
0.44770	0.06496	0.00856	-0.01158	0.99782	-0.00186
0.40729	0.06446	0.01202	-0.01351		
0.36991	0.06345	0.01579	-0.01525		
0.33534	0.06207	0.02399	-0.01827		
0.30335	0.06037	0.03308	-0.02088		
0.27375	0.05843	0.04297	-0.02324		
0.24636	0.05630	0.05369	-0.02543		
0.22101	0.05403	0.06534	-0.02753		
0.19756	0.05163	0.07802	-0.02959		
0.17585	0.04914	0.09182	-0.03161		
0.15578	0.04658	0.10685	-0.03361		
0.13720	0.04397	0.12326	-0.03559		
0.12004	0.04131	0.14114	-0.03752		
0.10415	0.03862	0.16066	-0.03939		
0.08949	0.03590	0.18201	-0.04117		
0.07597	0.03315	0.20540	-0.04283		
0.06350	0.03037	0.23108	-0.04429		
0.05203	0.02754	0.25934	-0.04550		
0.04147	0.02465	0.29052	-0.04637		
0.03176	0.02163	0.32505	-0.04677		

Appendix B List of test cases and design variables

The following hybrid airfoils were designed and tested at the given conditions for this research

Table B.1 Hybrid Airfoil Design Variables and Test Cases

Case	Span Section	SF	Lower LE Extent	Type	C_{m0}	Nose Droop	Flap Angle	α_D	Notes
1	60%	3	10%	Cambered	-0.18	-2.00	0°	2°	Baseline Case
2	22%	1			Full Scale			2°	
3	60%	1			Full Scale			2°	
4	90%	1			Full Scale			2°	
5	22%	3	10%	Cambered	-0.15	-0.50	0°	2°	Inboard Airfoil
6	90%	3	10%	Cambered	-0.20	-2.50	0°	2°	Outboard Airfoil
7	60%	3	3%	Cambered	-0.18	-2.00	0°	2°	3%LE
8	60%	3	5%	Cambered	-0.18	-2.00	0°	2°	5% LE
9	60%	3	15%	Cambered	-0.18	-2.00	0°	2°	15% LE
9	60%	2	10%	Cambered	-0.10	-2.20	0°	2°	Larger Scale
10	60%	4	5%	Cambered	-0.27	-1.80	0°	2°	Smaller Scale
11	60%	5	5%	Cambered	-0.30	-1.50	0°	2°	Smallest Scale
12	60%	3	10%	Cambered	-0.20	-3.30	0°	4°	Change in Alpha
13	60%	1			Full Scale			4°	
14	60%	3	10%	Cambered	-0.25	-4.20	0°	6°	
15	60%	1			Full Scale			6°	
16	60%	1			Full Scale			0°	
17	60%	3	10%	Cambered	-0.15	-0.50	0°	0°	
18	60%	3	10%	Flapped	0.00	0.00	3°	0°	
19	60%	3	10%	Flapped	0.00	0.00	7°	2°	Matched flap
20	60%	3	10%	Flapped	0.00	0.00	9°	4°	
21	60%	3	10%	Flapped	0.00	0.00	17°	6°	
22	60%	3	10%	Cambered	-0.18	-2.00	0°	2°	40 µm Large Droplet
23	60%	3	10%	Cambered	-0.18	-2.00	0°	2°	-13° Lower Temp
24	60%	3	10%	Cambered	-0.18	-2.00	0°	2°	10 ft Tunnel
25	22%	3	10%	Cambered	-0.15	-0.50	0°	2°	10 ft Tunnel
26	90%	3	10%	Cambered	-0.20	-2.50	0°	2°	10 ft Tunnel
27	60%	1			Full Scale			2°	10 ft Tunnel
28	60%	3	10%	Cambered	-0.18	-2.00	0°	2°	3 ft Tunnel
29	60%	3	10%	Cambered	-0.18	-2.00	0°	2°	5 ft Tunnel
30	60%	3	10%	Cambered	-0.18	-2.00	0°	2°	7 ft Tunnel
31	60%	3	10%	Cambered	-0.18	-2.00	0°	2°	20 ft Tunnel
32	60%	3	10%	Cambered	-0.18	-2.00	1°	2°	Tunnel Flap adjustment
33	60%	3	10%	Cambered	-0.18	-2.00	-4°	0°	Alpha flap adjustment
34	60%	3	10%	Cambered	-0.18	-2.00	8°	6°	

References

[1] Bragg, M.B., Broeren, A.P, Blumenthal, L.A. “Iced-Airfoil Aerodynamics”, *Progress in Aerospace Sciences*, Vol. 41, No. 5, pg. 323–418. 2005.

[2] Anderson, D. N., “Manual of Scaling Methods”. NASA CR-2004-21287.

[3]Von Glahn, U.H., “Use of Truncated Flapped Airfoils for Impingement and Icing Tests of Full-Scale Leading-Edge Sections,” NACA/RM E56E11, 1956.

[4] Saeed, F., Selig, M.S., Bragg, M.B., “Design of Subscale Airfoils with Full Scale Leading Edges for Ice Accretion Testing”, *AIAA Journal of Aicraft,* Vol. 34, No. 1, pg. 94-100. 1997.

[5] Selig, M.S. Mauhmer, M.D., “Multipoint Inverse Airfoil Design Method Based on Conformal Mapping” *AIAA Journal*, Vol. 30, No. 5, pg. 1162-1170. 1992.

[6] AIRDROP, Bragg, M.B., Urbana, IL, 1990.

[7]Saeed, F., Selig, M.S., and Bragg, M.B., “Hybrid Airfoil Design Method to Simulate Full-Scale Ice Accretion Throughout a Given α Range” *AIAA Journal of Aircraft*, Vol. 35, No.2, pg. 233-239, 1998.

[8] Saeed, F., Selig, M.S., Bragg, M.B., “Hybrid Airfoil Design Procedure Validation for Full-Scale Ice Accretion Simulation”, *AIAA Journal of Aircraft,* Vol. 36, No.5, pg. 769-776. 1999.

[9] Bragg, M.B., Broeren, A., Addy, H., Potapczuk, M., Guffond, D., Monteruil, E., “Airfoil Ice-Accretion Aerodynamics Simulation”, AIAA, Urbana, IL, 2007.

[10] Broeren, A.P., Bragg, M.B., Addy, H.E., Lee, S., Moens, F., Guffond, D., “Effect of High-Fidelity Ice-Accretion Simulations on Full-Scale Airfoil Performance” *AIAA Journal of Aircraft*, Vol. 47, No.1, pg. 240-254. 2010.

[11] Vassberg, J.C., DeHaan, M.A., Rivers, S.M., Wahls, R.A., ”Development of a Common Research Model for Applied CFD Validation Studies,” AIAA-2008-6919, 2008.

[12] Rivera, M.B., Dittberner, A., “Experimental Investigation of the NASA Common Research Model” *AIAA Applied Aerodynamics Conference,* AIAA, Chicago. 2010.

[13]Pro/ENGINEER, Version , PTC, Needham, MA,

[14]XFOIL, Version 6.9, Drela, M. and Youngren, H., Boston, MA, 2001.

[15]XFLR5, Version 6.06, Deperrois A., 2012

[16]Wright, W.B., “User Manual for the NASA Glenn Ice Accretion Code LEWICE Version 2.2.2”, NASA/CR-2002-211793, 2002.

[17]Drela, M., “XFOIL: An Analysis and Design System for Low Reynolds Number Airfoils,” MIT Dept. of Aeronautics and Astronautics, 1989.

[18]Meschia,F. “Model analysis with XFLR5,” *R/C Soaring Digest,* Vol. 25, No. 2, pg. 27-51. 2008.

[19]PROFOIL A Multipoint Inverse Airfoil Design Method, Version 2.0, Selig, M.S., Champaign, IL, 1999.

[20] TUNDROP, Wells, S. Urbana, IL. 1992.

[21]Ruff, G.A. “Quantitative Comparison of Ice Accretion Shapes,” *AIAA Journal of Aircraft,* Vol. 39, No. 2, pg. 418-426. 2002

[22] Bragg M.B., Wells, Stephen L. “Effect of Wind-Tunnel Walls on Airfoil Droplet Impingement*”*; *AIAA Journal of Aircraft*, Vol 31, No.1, pg. 175-180. 1994.

[23] Barlow, J.B., Rae, W.H, and Pope.A. *Low Speed Wind Tunnel Testing*, 3rd Edition, Wiley-India Pvt. Ltd. New Delhi, 2010, Chap. 9